

Dust Dynamics in AGN Winds: A New Mechanism For Multiwavelength AGN Variability

Nadine H. Soliman¹, Philip F. Hopkins¹

¹ *TAPIR, Mailcode 350-17, California Institute of Technology, Pasadena, CA 91125, USA*

Accepted XXX. Received YYY; in original form ZZZ

ABSTRACT

Partial dust obscuration in active galactic nuclei (AGN) has been proposed as a potential explanation for some cases of AGN variability. The dust-gas mixture present in AGN torii is accelerated by radiation pressure leading to the launching of an AGN wind. Dust under these conditions has been shown to be unstable to a generic class of fast growing resonant drag instabilities (RDIs). We present the first set of numerical simulations of radiation driven outflows that include explicit dust dynamics in conditions resembling AGN winds and discuss the implications of the RDIs on the morphology of the AGN torus, AGN variability, and the ability of the radiation to effectively launch a wind. We find that the RDIs rapidly develop reaching saturation at times much shorter than the global timescales of the outflows, resulting in the formation of filamentary structure on box-size scales with strong dust clumping and super-Alfvénic velocity dispersions on micro-scales. This results in 10-20% fluctuations in dust opacity and gas column density, integrated along mock observed lines-of-sight to the quasar accretion disk, over year to decade timescales with a red-noise power spectrum which is commonly observed for AGN. Additionally, all our simulations show that the radiation is sufficiently coupled to the dust-gas mixture launching highly super-sonic winds, which entrain 70-90% of gas, with a factor of $\lesssim 3$ photon momentum loss relative to the ideal case. Therefore, the RDIs could play an important role in generating the clumpy nature of AGN torii and driving AGN variability consistent with observations.

Key words: instabilities — turbulence — ISM: kinematics and dynamics — star formation: general — galaxies: formation — dust, extinction

1 INTRODUCTION

Dust plays a critical role in how a wide range of astrophysical systems form, evolve, and are observed. It is involved in processes such as planetary and stellar formation and evolution; chemical evolution, heating, and cooling in the interstellar medium (ISM); and feedback and outflow launching in star-forming regions, cool stars and active galactic nuclei (AGN) (Draine 2003; Dorschner 2003; Apai & Lauretta 2010; Höfner & Olofsson 2018). Moreover, dust imprints ubiquitous observable signatures, such as the attenuation and extinction of observed light.

One particular regime where dust is believed to play a central role in both dynamics and observations is the “dusty torus” region around AGN (Antonucci 1982; Lawrence & Elvis 1982; Urry & Padovani 1995). It is well established that outside of the dust sublimation radius, AGN and quasars are surrounded by a dust-laden region with extinction and column densities ranging from $\sim 10^{22}$ cm⁻² in the polar direction to $\sim 10^{26}$ cm⁻² in the midplane (on average), exhibiting “clumpy” sub-structure in both dust and gas, ubiquitous time variability on \gtrsim yr timescales, and a diverse array of detailed geometric and reddening properties (see Krolik & Begelman 1988; Elitzur & Shlosman 2006; Tristram et al. 2007; Nenkova et al. 2008b,a; Stalevski et al. 2012, or for recent reviews see Netzer 2015; Padovani et al. 2017; Hickox & Alexander 2018; Baloković et al. 2018), as well as

a broad variety of different extinction curve shapes (Laor & Draine 1993; Hopkins et al. 2004; Maiolino et al. 2004; Hatziminaoglou et al. 2009; Gallerani et al. 2010; Hönic & Kishimoto 2010). It has been recognized for decades that the torus represents one (of several) natural locations where bright AGN should drive outflows, and indeed many have gone so far as to propose the “torus” is, itself, an outflow (see e.g. Sanders et al. 1988; Norman & Scoville 1988; Pier & Krolik 1992; Konigl & Kartje 1994; Elvis 2000; Elitzur & Shlosman 2006; Murray et al. 2005). Put simply, because the dust cross-section to radiation scattering and absorption is generally much larger than the Thompson cross section, which defines the Eddington limit, any AGN accreting at even modest fractions of Eddington should be able to unbind material via radiation pressure on dust, launching strong outflows. This concept has led to an enormous body of detailed observational followup (Hönic & Kishimoto 2010; Horst et al. 2008; Tristram et al. 2009; Bianchi et al. 2009; Alonso-Herrero et al. 2011; Kishimoto et al. 2011; Ricci et al. 2017; Hönic 2019) and detailed theoretical simulations and models of dust-radiation-pressure driven outflows from AGN in the torus region (Thompson et al. 2005; Debuhr et al. 2010; Wada et al. 2009; Wada 2012; Roth et al. 2012; Costa et al. 2018; Thompson et al. 2015; Ishibashi & Fabian 2015; Chan & Krolik 2016; Baskin & Laor 2018; Ishibashi et al. 2018; Kawakatu et al. 2020).

Yet despite this extensive literature, almost all the theoretical work

discussed above has assumed that the dust dynamics are perfectly coupled to the dynamics of the surrounding gas – effectively that the two “move together” and the dust (even as it is created or destroyed) can simply be treated as some “additional opacity” of the gas. But in reality, radiation absorbed/scattered by grains accelerates those grains, which then interact with gas via a combination of electromagnetic (Lorentz, Coulomb) and collisional (drag) forces, re-distributing that momentum.

Accurately accounting for these interactions is crucial for understanding any radiation-dust-driven outflows. If the dust “free-streaming length” is very large, grains could simply be expelled before sharing their momentum with gas (Elvis et al. 2002). If dust can be pushed into channels, creating low-opacity sightlines through which radiation can leak out efficiently, some authors have argued that the coupled photon momentum might be far smaller than the standard expectation $\sim \tau L/c$ (where τ is the infrared optical depth; see Krumholz & Thompson 2012 but also Kuiper et al. 2012; Wise et al. 2012; Tsang & Milosavljević 2015).

Perhaps most importantly, Squire & Hopkins (2018b) showed that radiation-dust driven outflows are generically unstable to a generic class of “resonant drag instabilities” (RDIs), which occur whenever there is any difference in the forces acting on dust versus gas. In subsequent work (Hopkins & Squire 2018b; Squire & Hopkins 2018a; Hopkins & Squire 2018a) they showed that systems like radiation-dust driven outflows are unstable to the RDIs on all wavelengths – even scales much larger than the dust free-streaming length or mean free path. Subsequent idealized simulations of these instabilities (Moseley et al. 2019; Seligman et al. 2019a; Hopkins & Squire 2018a) have shown that they can grow rapidly, reaching significant non-linear amplitudes on large scales, driving clumping and time-dependent clustering in both dust and gas, and grain-size dependent separation of dust and gas.

This could therefore be critical not just for understanding whether or not an outflow is launched in the first place, but to explaining various phenomena above such as clumping in the torus, variations in AGN extinction curves, and certain forms of time variability. Specifically, while AGN are known to vary at essentially all wavelengths and timescales from hours through Gyr (Uttley & McHardy 2004; Paolillo et al. 2004, 2017; Assef et al. 2018; Caplar et al. 2017), variation in their X-ray flux ($\sim 20\%$ to 80%) on timescales of a \sim a few years, without variation in the optical component has been reported for several sources (Risaliti et al. 2002, 2005; Markowitz et al. 2014; Laha et al. 2020; De Rosa et al. 2007; Smith & Vaughan 2007). In certain cases, ‘changing-look’ AGN, order of magnitude variability has been observed on timescales as short as a few days to a couple hours (e.g., LaMassa et al. 2015; Runnoe et al. 2016; Ruan et al. 2016; McElroy et al. 2016; Yang et al. 2018; Mathur et al. 2018; Wang et al. 2018; Stern et al. 2018; Ross et al. 2020; Trakhtenbrot et al. 2019; Hon et al. 2020). However, the processes driving such variability and the clumpy nature of the torus remain unexplained.

In the paper, we therefore explore radiation-dust driven outflows for AGN torii including for the first time explicit dust-gas radiation dynamics. Firstly, in §2, we introduce the numerical methods and initial conditions of the simulations. In §3, we present an analysis of our results. We analyze the morphology, dynamics, and non-linear evolution of the dusty gas in the simulations. In §3.5 we compare the results of our standard simulations to simulations with full radiation-dust-magnetohydrodynamics. Further, in §3.6 we discuss whether radiation-driven outflows could be successfully launched and quantify the momentum coupling efficiency within the wind. We consider how the presence of the RDIs affects observable AGN properties in

§3.9 such as time variability. Finally, we summarize our findings in §4.

2 METHODS & PARAMETERS

We consider an initially vertically-stratified mixture of magnetized gas (obeying the ideal MHD equations) and an observationally-motivated spectrum of dust grains with varying size, mass, and charge, coupled to one another via a combination of electromagnetic and collisional/drag forces, in an external gravitational field, with the dust absorbing and scattering radiation from an external source. In Figure 1, we show a cartoon illustrating the geometry of our idealized setup and its relation to an AGN torus.

2.1 Numerical Methods

The numerical methods for our simulations are identical to those in Hopkins et al. (2022), to which we refer for more details (see also Hopkins & Lee 2016; Lee et al. 2017; Moseley et al. 2019; Seligman et al. 2019b; Hopkins et al. 2020b; Steinwandel et al. 2021; Ji et al. 2021; Squire et al. 2022 for additional details and applications of these methods). Briefly, we run our simulations with the code GIZMO¹ (Hopkins 2015), utilizing the Lagrangian “meshless finite mass method” (MFM) to solve the equations of ideal magnetohydrodynamics (MHD; Hopkins & Raives 2016; Hopkins 2016, 2017; Su et al. 2017). Dust grains are modeled as “super-particles” (Carballido et al. 2008; Johansen et al. 2009; Bai & Stone 2010; Pan et al. 2011; McKinnon et al. 2018) where each simulated “dust particle” represents an ensemble of dust grains with a similar grain-size (ϵ_{grain}), charge (q_{grain}), and mass (m_{grain}).

We simulate a 3D box with a base of length $H_{\text{gas}} = L_{xy}$ in the xy plane and periodic \hat{x} , \hat{y} boundaries, and height $L_{\text{box}} = L_z = 20 L_{xy}$ in the \hat{z} direction with a reflecting lower ($z = 0$) and outflow upper ($z = +L_z$) boundary. Dust and gas feel a uniform external gravitational field $\mathbf{g} = -g \hat{z}$. The gas has initial uniform velocity $\mathbf{u}_g^0 = 0$, initial magnetic field $\mathbf{B}_0 \equiv B_0 \hat{\mathbf{B}}_0$ in the xz plane ($\hat{\mathbf{B}}_0 = \sin(\theta_B^0) \hat{x} + \cos(\theta_B^0) \hat{z}$), obeys a strictly isothermal equation of state ($P = \rho_g c_s^2$), and the initial gas density is stratified with $\rho_g^0 \equiv \rho_g(t = 0) = \rho_{\text{base}} \exp(-z/H_{\text{gas}})$ (with $\rho_{\text{base}} \approx M_{\text{gas, box}}/H_{\text{gas}}^3$).

Each dust grain obeys an equation of motion

$$\begin{aligned} \frac{d\mathbf{v}_d}{dt} &= \mathbf{a}_{\text{gas, dust}} + \mathbf{a}_{\text{grav}} + \mathbf{a}_{\text{rad}} \\ &= -\frac{\mathbf{w}_s}{t_s} - \frac{\mathbf{w}_s \times \hat{\mathbf{B}}}{t_L} + \mathbf{g} + \frac{\pi \epsilon_{\text{grain}}^2}{m_{\text{grain}} c} \langle Q \rangle_{\text{ext}} \mathbf{G}_{\text{rad}} \end{aligned} \quad (1)$$

where \mathbf{v}_d is the grain velocity; $\mathbf{w}_s \equiv \mathbf{v}_d - \mathbf{u}_g$ is the drift velocity for a dust grain with velocity \mathbf{v}_d and gas velocity \mathbf{u}_g at the same position \mathbf{x} ; \mathbf{B} is the local magnetic field; $\mathbf{a}_{\text{gas, dust}} = -\mathbf{w}_s/t_s - \mathbf{w}_s \times \hat{\mathbf{B}}/t_L$ includes the forces from gas on dust including drag (in terms of the “stopping time” t_s) and Lorentz forces (with gyro/Larmor time t_L); $\mathbf{a}_{\text{grav}} = \mathbf{g}$ is the external gravitational force; and \mathbf{a}_{rad} is the force from radiation in terms of the grain-size ϵ_{grain} , mass $m_{\text{grain}} \equiv (4\pi/3) \bar{\rho}_{\text{grain}}^i \epsilon_{\text{grain}}^3$ (in terms of the internal grain density $\bar{\rho}_{\text{grain}}^i$), dimensionless absorption+scattering efficiency $\langle Q \rangle_{\text{ext}}$, speed of light c , and radiation field $\mathbf{G}_{\text{rad}} \equiv \mathbf{F}_{\text{rad}} - \mathbf{v}_d \cdot (e_{\text{rad}} \mathbb{I} + \mathbb{P}_{\text{rad}})$ in terms of the radiation flux/energy density/pressure density \mathbf{F}_{rad} , e_{rad} , \mathbb{P}_{rad} .

¹ A public version of the code is available at <http://www.tapir.caltech.edu/~phopkins/Site/GIZMO.html>

The dust is initialized with the local homogeneous steady-state equilibrium drift and a spatially-uniform dust-to-gas ratio $\rho_d^0 = \mu^{\text{dg}} \rho_g^0$. For all forces “from gas on dust” $a_{\text{gas, dust}}$ the gas feels an equal-and-opposite force (“back-reaction”). The dust gyro time is given in terms of the grain charge $q_{\text{grain}} = Z_{\text{grain}} e$ as $t_L \equiv m_{\text{grain}} c / |q_{\text{grain}} \mathbf{B}|$, and for the parameter space of our study the drag is given by Epstein drag (as opposed to Coulomb or Stokes drag) with

$$t_s \equiv \sqrt{\frac{\pi \gamma \bar{\rho}_{\text{grain}}^i \epsilon_{\text{grain}}}{8 \rho_g c_s}} \left(1 + \frac{9\pi \gamma |\mathbf{w}_s|^2}{128 c_s^2} \right)^{-1/2}, \quad (2)$$

We adopt a standard empirical Mathis et al. (1977) power-law grain-size spectrum with differential number $dN_d/d\epsilon_{\text{grain}} \propto \epsilon_{\text{grain}}^{-3.5}$ with a range of a factor of 100 in grain-size ($\epsilon_{\text{grain}}^{\text{max}} = 100 \epsilon_{\text{grain}}^{\text{min}}$). We assume the grain internal density/composition is independent of grain-size, and assume the charge-to-mass ratio scales as $|q_{\text{grain}}|/m_{\text{grain}} \propto \epsilon_{\text{grain}}^{-2}$, consistent with grains charged by a range of processes relevant in this regime such as collisions, Coulomb, photoelectric, or electrostatically-limited processes (Draine & Sutin 1987; Tielens 2005).

As in Hopkins et al. (2022), we consider two different treatments of the radiation fields. Given the range of column densities we will explore, we are interested in the multiple-scattering regime, or equivalently Rayleigh scattering. In this regime, the radiation should be in the long-wavelength limit (spectrum peaked at wavelengths $\langle \lambda_{\text{rad}} \rangle \gg \epsilon_{\text{grain}}$), so we expect and assume the spectrally-averaged $\langle Q \rangle_{\text{ext}} \propto \epsilon_{\text{grain}}$, and we approximate the radiation with a single band (spectrally-integrated), so effectively treat the grains as introducing a grain-size-dependent but otherwise “gray” isotropic scattering opacity. In our first simplified treatment (our “constant flux” simulations), we assume the radiation fields obey their homogeneous equilibrium solution, giving $\mathbf{G}_{\text{rad}} \approx \mathbf{F}_{\text{rad}} \approx \mathbf{F}_0 = F_0 \hat{z}$. This is a reasonable approximation so long as the radiation is not “trapped” in highly-inhomogeneous dust clumps. But we also run a subset of “full radiation-dust-magnetohydrodynamic” (RDMHD) simulations where the radiation field is explicitly evolved using to the full M1 radiation-hydrodynamics treatment in GIZMO (Lupi et al. 2017, 2018; Hopkins & Grudić 2019; Hopkins et al. 2020a; Grudić et al. 2021), including terms to $O(v^2/c^2)$: $\partial_t e_{\text{rad}} + \nabla \cdot \mathbf{F}_{\text{rad}} = -R_{\text{dust}} \mathbf{v}_d \cdot \mathbf{G}_{\text{rad}}/c^2$, $\partial_t \mathbf{F}_{\text{rad}} + c^2 \nabla \cdot \mathbb{P}_{\text{rad}} = -R_{\text{dust}} \mathbf{G}_{\text{rad}}$, where the absorption/scattering coefficients R_{dust} are calculated directly from the explicitly-resolved dust grain populations (consistent exactly with the radiation flux they see in \mathbf{a}_{rad}).

Our default simulation parameter survey adopts 10^6 gas cells and 4×10^6 dust super-particles. And unless otherwise specified, our analysis uses the “full RDMHD” simulations. Readers interested in details should see Hopkins et al. (2022). In that paper, we applied these numerical methods to simulations of radiation-dust-driven outflows in molecular clouds and HII regions. The key differences are (1) we consider a very different parameter space (much higher densities and stronger radiation fields), which lead to qualitatively different instabilities and behaviors, and (2) we specifically model the multiple-scattering regime, while Hopkins et al. (2022) focused only on the single-scattering limit.

2.2 Parameter Choices

Our simulations are then specified by a set of constants (size and charge of the largest grains, dust-to-gas ratio, radiation flux, etc.). To motivate these, we consider a fiducial case of dust around a bright quasar. We expect the most dramatic effects of radiation on dust at the distances closest to the black hole where grains can survive, i.e. just

outside the dust sublimation radius $r_{\text{sub}} \sim (L_{\text{QSO}}/4\pi\sigma_{\text{SB}}T_{\text{sub}}^4)^{1/2}$ where $T_{\text{sub}} \sim 2000$ K is the dust sublimation temperature and we will consider a typical quasar with $L_{\text{QSO}} \sim 10^{46}$ erg s $^{-1}$ (i.e. $M_{\text{B}} \sim -24$, a typical $\sim L_*$ or modestly sub- L_* QSO at redshifts $z \sim 1-6$; see Shen et al. 2020), so $r_{\text{sub}} \sim 0.3$ pc and this corresponds to a BH of mass $M_{\text{BH}} \sim \times 10^8 M_{\odot}$ accreting near its Eddington limit.

We then take $H_{\text{gas}} \sim r_{\text{sub}}$, $F_0 \sim L_{\text{QSO}}/(4\pi r_{\text{sub}}^2)$, $g \sim GM_{\text{BH}}/r_{\text{sub}}^2$, a standard dust-to-gas ratio $\mu^{\text{dg}} = 0.01$ (see references in § 1), typical $\bar{\rho}_{\text{grain}}^i \sim 1.5$ g cm $^{-3}$ and absorption efficiency for the largest grains $\langle Q \rangle_{\text{ext}} (\epsilon_{\text{grain}} = \epsilon_{\text{grain}}^{\text{max}}) \sim 0.2$ (Draine & Lee 1984), and initial magnetic field strength given by a plasma $\beta_0 \equiv (c_s/v_A[z=0])^2 = 4\pi\rho_{\text{base}}(c_s/B_0)^2 \sim 1$ with an arbitrary angle $\theta_B^0 = \pi/4$ (though this is essentially a nuisance parameter here). We consider various values of $\epsilon_{\text{grain}}^{\text{max}}$ from $0.01 \mu\text{m}$ (smaller grains than typical in the diffuse ISM) through $1 \mu\text{m}$ (larger), and also explore variations in the gas density parameterized via the gas column density integrated through the box to infinity, $N_{\text{H, gas}} \equiv m_p^{-1} \int \rho_g^0 dz = \rho_{\text{base}} H_{\text{gas}}/m_p \sim 10^{22} - 10^{26}$ cm $^{-2}$, representative of observed values through different lines-of-sight of angles through the AGN torus.

The one remaining parameter is the dust charge. We have considered both (a) cases where the grains are strongly shielded and the gas neutral/cold, so collisional charging dominates, and (b) cases where some photo-electric (non-ionizing UV) flux is able to reach the grains. Given the scalings for grain charge in both regimes (Tielens 2005; Draine & Sutin 1987), if even a small fraction of the QSO photo-electric flux reaches grains they will generally reach the electrostatic photoelectric charging limit $Z_{\text{grain}} \sim \langle Z \rangle_{\text{max}} \sim 5000$ ($\epsilon_{\text{grain}}/\mu\text{m}$) (Tielens 2005). For simplicity, we adopt this by default, but using instead the collisional charge expression from Draine & Sutin (1987), which decreases $|Z_{\text{grain}}|$ significantly, has little effect, because we find that the magnetic grain-gas interactions (grain charge effects) are sub-dominant in the parameter space of interest even with the larger $|Z_{\text{grain}}|$. We include a table in Appendix A which lists the specific parameters for each simulation.

3 RESULTS

3.1 Analytic Expectations & Background

As discussed in Hopkins & Squire (2018b,a), the behavior of an unstable RDI mode with wave-number \mathbf{k} in a dust-gas mixture like those we simulate is characterized by the dimensionless parameter $\mathbf{k}\langle w_s \rangle \langle t_s \rangle$. This parameter then defines three regimes of the instabilities,

$$\begin{cases} \mathbf{k}\langle w_s \rangle \langle t_s \rangle \lesssim \mu^{\text{dg}} & \text{(Low-k, long-wavelength)} \\ \mu^{\text{dg}} \lesssim \mathbf{k}\langle w_s \rangle \langle t_s \rangle \lesssim (\mu^{\text{dg}})^{-1} & \text{(Mid-k, intermediate wavelength)} \\ \mathbf{k}\langle w_s \rangle \langle t_s \rangle \gtrsim (\mu^{\text{dg}})^{-1} & \text{(High-k, short-wavelength)}. \end{cases} \quad (3)$$

Rewriting the parameter in terms of wavelength, we can see that $\lambda_{\text{crit}} \sim (\bar{\rho}_{\text{grain}}^i \epsilon_{\text{grain}})/(\mu^{\text{dg}} \rho_g) \sim \tilde{\alpha} H_{\text{gas}}/\mu^{\text{dg}}$ defines the critical wavelength above which modes are in the low-k regime, where $\tilde{\alpha} \equiv (\bar{\rho}_{\text{grain}}^i \epsilon_{\text{grain}})/(\rho_{\text{base}} H_{\text{gas}})$ is the dimensionless grain-size parameter. For the parameter set explored here, $\tilde{\alpha} \ll \mu^{\text{dg}}$, we find that largest-wavelength interesting modes ($\lambda \sim H_{\text{gas}} \gg \lambda_{\text{crit}}$) always lie in the “long-wavelength” regime. Within the linear theory framework presented in Hopkins & Squire (2018b), this mode behaves as

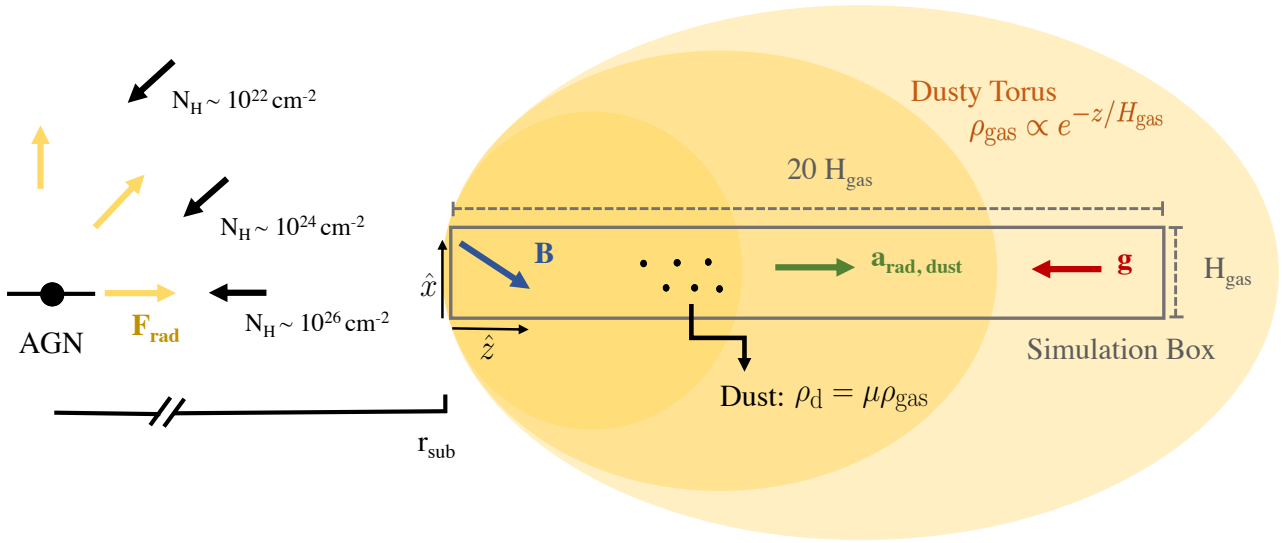


Figure 1. Cartoon illustrating our simulation setup. We simulate 3D boxes of size $H_{\text{gas}} \times H_{\text{gas}} \times 20 H_{\text{gas}}$ along the \hat{x} , \hat{y} and \hat{z} directions respectively with $\sim 10^6$ resolution elements. We enforce outflow upper and reflecting lower boundary conditions with periodic sides. The gas and dust are initially stratified such that $\rho_{\text{gas}} \propto e^{-z/H_{\text{gas}}}$, and $\rho_{\text{d}} = \mu_0^{\text{dg}} \rho_{\text{gas}}$ where $\mu_0^{\text{dg}} = 0.01$ corresponding to a uniform dust-to-gas ratio. The gas follows an isothermal ($\gamma = 1$) EOS with sound speed c_s , an initial magnetic field $\mathbf{B}_0 = |\mathbf{B}|(\sin\theta_B^0 \hat{x} + \cos\theta_B^0 \hat{z})$ in the $\hat{x} - \hat{z}$ plane and gravitational acceleration $\mathbf{g} = -g\hat{z}$. The dust grains are modeled as super-particles each representing a population of grains of a given size sampled from a standard MRN spectrum with factor = 100 range of sizes. The grains are photo-electrically charged, with charge appropriately scaled according to grain-size. They experience an upward acceleration $a_{\text{rad,dust}}$ due to absorption of an initial upward radiation flux $F_0 = +F_0 \hat{z}$ corresponding to radiation from an AGN located a sublimation radius r_{sub} distance away, and are coupled to the gas through drag and Lorentz forces. We consider a range of $10^{22} - 10^{26} \text{ cm}^{-2}$ in column densities representing different lines-of-sight angles through the dusty torus.

a "compressible wave", with similar dust and gas velocity perturbations that are nearly in phase and parallel to the wave-vector $\hat{\mathbf{k}}$. This will therefore drive relatively weak dust-gas separation with respect to other regimes previously studied in [Hopkins et al. \(2022\)](#). The linear growth timescale t_{grow} of the fastest growing modes in this regime scales approximately as:

$$t_{\text{grow}}(k) \sim \frac{1}{\mathfrak{F}(k)} \sim \left(\frac{\mu^{\text{dg}} \mathbf{w}_s^2 k^2}{t_s} \right)^{-1/3}, \quad (4)$$

where $\mathfrak{F}(k)$ is the linear growth rate for a mode with wave-number k ([Hopkins & Squire 2018b](#)). Importantly, as shown therein, the fastest growing mode in the linear long-wavelength regime is the "pressure free" mode, which is weakly dependent on the magnetization and thermal physics of the gas. We discuss this further below. As shown in figure 2, the resonant modes initially appear with a preferential angle as predicted by linear theory, but the outflow eventually drives them to form vertical filaments.

We define the geometrical optical depth τ_{geo} instead of the "observed" optical depth τ_{λ} , since the latter depends on the observed wavelength (the same integral replacing $\pi \epsilon_{\text{grain}}^2 \rightarrow Q_{\lambda}(\epsilon_{\text{grain}}, \lambda) \pi \epsilon_{\text{grain}}^2$), integrated from the base of the box to infinity. Assuming a vertically stratified environment and dust grains with a power-law grain-size spectrum, we can express τ_{geo} strictly in terms of our simulation parameters,

$$\tau_{\text{geo}} \equiv \int_0^{\infty} \pi \epsilon^2 n_{\text{grain}} dz \quad (5)$$

$$= C \mu^{\text{dg}} \frac{\rho_g H_{\text{gas}}}{\rho_d \epsilon_{\text{grain}}^{\text{max}}} = C \left(\frac{\mu^{\text{dg}}}{\tilde{\alpha}_m} \right), \quad (6)$$

$$(7)$$

where $\tilde{\alpha}_m$ is the maximum grain-size parameter ($\tilde{\alpha}$ evaluated at $\epsilon_{\text{grain}} = \epsilon_{\text{grain}}^{\text{max}}$), and the constant $C \sim 20$.

Another useful parameter is the "free streaming length" of the dust (relative to the gas),

$$\frac{\ell_{\text{stream,dust}}}{H_{\text{gas}}} \sim 10^{-4} \left(\frac{\epsilon_{\text{grain}}}{\mu\text{m}} \right) \left(\frac{10^{24} \text{ cm}^{-2}}{N_{\text{H,gas}}} \right). \quad (8)$$

In short, for all our simulations, grains are "well-coupled" to the gas in the sense that $\ell_{\text{stream,dust}} \ll H_{\text{gas}}$, so we do not expect them to simply "eject" from the gas without interacting and sharing momentum.

3.2 Parameters & Physics with Weak Effects

We now discuss physical parameters that we tested, but found to have weak to no effect on the behavior of the instabilities within this regime including: magnetic field strength, magnetic field direction, AGN luminosity, grain charge, and strength of gravity.

3.2.1 Charging Physics & Magnetic Field Strength

We ran tests varying the magnetic field strength B_0 , or equivalently the plasma β , and magnetic field orientation θ_B within the box. Similarly, as the grain charge is unconstrained, we consider different grain charging mechanisms (collisional vs. photoelectric), and found these parameters to have a negligible effect on the long-term behavior of the instabilities. This is due to two reasons. Firstly, this arises naturally within AGN-like environments where Lorentz forces are weak relative to the drag force, i.e. $\tau \equiv t_s/t_L \sim \tilde{\phi}_m/\tilde{a}_d^{1/2} \ll 1$ throughout our parameter space. Secondly, the dominant modes in our simulations are in the "long-wavelength regime" are only weakly sensitive

to magnetic effects as the magnetic pressure and tension provide only second order corrections to what is to leading order a “collisionless” or “pressure-free” mode (Hopkins & Squire 2018a). Therefore, we observe that at early stages of the RDIs’ development, amplified magnetic fields, or higher grain charge to mass ratios merely result in density perturbations propagating at slightly different angles $\sim \theta_B$, but the fluid flow retains its general properties. Further, as the instabilities reach the non-linear stage of their evolution, this propagation angle decreases till the fluid is moving roughly parallel to the vertical acceleration, and we see essentially no effect on the medium.

3.2.2 Thermal State of Gas

We find that the choice of the thermal equation-of-state of the gas γ , and therefore the speed of sound c_s do not affect our results. As the grains are accelerated to super-sonic velocities, c_s factors out of the relevant equations such as the stopping time and the growth rates of the modes to leading order in the linear theory for these particular long-wavelength mode of interest.

3.2.3 Gravity

Further, as shown in Table A1, the strength of gravity is much weaker than the acceleration due to radiation within the regime under investigation, i.e. $\tilde{g}/\tilde{a}_d \sim 10^{-3} (\epsilon_{\text{grain}}^{\text{max}}/\mu\text{m})$ for our choice of parameters. Thus, gravity acts merely to ensure that the gas that is left behind the wind “falls back”, but does not have a noticeable effect on the general behavior of the RDIs. It is easy to verify that for the conditions and timescales we emulate here, self-gravity of the gas should also be unimportant.

3.2.4 AGN Luminosity

Naively, the AGN luminosity should have an important effect here. However, in the dimensionless units in which we will work, i.e. length in units of $\sim H_{\text{gas}} \sim r_{\text{sub}}$, time in units of the “acceleration time” defined below, the absolute value of the AGN luminosity factors out completely. So while the AGN luminosity does not affect the qualitative behavior of the RDIs (in the appropriate units), it effectively defines characteristic time and spatial scales of the problem. For example, the AGN luminosity normalizes the sublimation radius, i.e. $r_{\text{sub}} \sim 0.3 \text{ pc } L_{46}^{1/2}$. This means if we define the flux at the base of our box as the flux at r_{sub} (as we do), the AGN luminosity factors out (the flux at r_{sub} is, by definition, fixed), and we find that the vertical acceleration of the column, $a_{\text{eff}} \equiv \mu^{\text{dg}} a_{\text{dust}}$, has the following scaling,

$$a_{\text{eff}} \sim 0.3 \text{ cm s}^{-2} \left(\frac{1 \mu\text{m}}{\epsilon_{\text{grain}}^{\text{max}}} \right),$$

which is independent of the AGN luminosity, and only depends on the maximum size of the grains.

The luminosity does however, normalize the bulk acceleration timescale which depends on both $H_{\text{gas}} \sim r_{\text{sub}}$ and a_{eff} , as

$$t_{\text{acc}} \equiv \sqrt{\frac{20 H_{\text{gas}}}{a_{\text{eff}}}} \\ \sim 245 \text{ yrs } L_{46}^{1/4} \left(\frac{\epsilon_{\text{grain}}^{\text{max}}}{\mu\text{m}} \right)^{1/2} \left(\frac{0.01}{\mu^{\text{dg}}} \right)^{1/2},$$

corresponding to the time when a perfectly coupled dust + gas fluid would have reached a height $z \sim 10 H_{\text{gas}}$. As we normalize our parameters to the sublimation radius r_{sub} and the bulk acceleration timescale t_{acc} , our findings are independent of the AGN luminosity. Nonetheless, if the luminosity was to increase at a fixed distance from the AGN source, the luminosity would not factor out from the equations of motion, and thus directly impact the evolution of the RDIs.

3.3 Parameters with Strong Effects

3.3.1 Grain-size and Column Density: The Geometric Optical Depth

Our results are sensitive to the choice of grain-size and column density. From Equation 3, we can see that the ratio of grain-size to column density determines the critical wavelength, and thus the ratio of the largest scale mode with $\lambda \sim H_{\text{gas}}$ to critical wavelength is

$$\frac{H_{\text{gas}}}{\lambda_{\text{crit}}} \sim \frac{H_{\text{gas}}}{\mathbf{w}_s t_s / \mu^{\text{dg}}} \sim \frac{\mu^{\text{dg}} H_{\text{gas}}}{\bar{\rho}_{\text{grain}}^i} \left(\frac{\rho_g}{\epsilon_{\text{grain}}} \right) \sim \frac{\mu^{\text{dg}}}{\tilde{\alpha}_m} = \frac{\tau_{\text{geo}}}{C} \quad (9) \\ \sim 300 (\mu^{\text{dg}}/0.01) (N_{\text{H}}/10^{24} \text{ cm}^{-2}) (1 \mu\text{m}/\epsilon_{\text{grain}}^{\text{max}}), \quad (10)$$

where $C \sim 20$ is a constant defined earlier.

Again, as $H_{\text{gas}}/\lambda_{\text{crit}} \gg 1$ for the typical values of $(\rho_g/\epsilon_{\text{grain}}^{\text{max}})$, the dominant modes are always in the long-wavelength regime. Also, the regime of the instabilities strictly depends on the geometrical optical depth. An environment with $\tau_{\text{geo}} \gtrsim 20$ would be sufficient to satisfy the criteria for the “long-wavelength RDI” regime.

Further, for this regime, we compare the instability growth time to the wind’s acceleration time,

$$\frac{t_{\text{acc}}}{t_{\text{grow}}} \sim 4.7 (H_{\text{gas}} \mathbf{k} \cdot \hat{\mathbf{w}})^{2/3} \left(\frac{\tilde{\alpha}_m}{\mu^{\text{dg}}} \right)^{1/6} \propto \tau_{\text{geo}}^{-1/6}. \quad (11)$$

Note that $H_{\text{gas}} \mathbf{k} \cdot \hat{\mathbf{w}} \sim 1$ and that $\mu^{\text{dg}}/\tilde{\alpha}_m \sim C\tau_{\text{geo}}$. Thus, the characteristic timescales and length-scales only depend on τ_{geo} or the ratio $N_{\text{H}}/\epsilon_{\text{grain}}^{\text{max}}$, yielding similar behaviors for similar ratios. As $t_{\text{acc}}/t_{\text{grow}} \propto \tau_{\text{geo}}^{-1/6}$, lower τ_{geo} (lower column density and larger grains) imply shorter growth times, i.e. more e-folding times for the clumping to amplify. Similarly, while lower dust-to-gas ratios would increase growth times $t_{\text{grow}} \propto (\mu^{\text{dg}})^{-1/3}$, it would increase the acceleration time more strongly $t_{\text{acc}} \propto (\mu^{\text{dg}})^{-1/2}$. These effects result in filaments with stronger clumping and higher variability. However, we note that this trend is weak $\sim \tau_{\text{geo}}^{1/6}$, so we observe similar levels of clumping/variability across the parameter space we explore.

3.4 General Profile of the Outflow and Large-scale Morphology

To understand how the RDIs affect the dynamics of the dusty torus, we first consider the resulting morphology within the region. In Figure 2, we show the temporal evolution of the gas (left) and the dust (right) column densities for a run with $N_{\text{H}} \sim 10^{24} \text{ cm}^{-2}$ and $\epsilon_{\text{grain}} \sim 1 \mu\text{m}$ in the x-z plane within $z \sim 0 - 9 H_{\text{gas}}$ at $t \sim (0, 0.3, 0.5) t_{\text{acc}}$. The plots show the radiation-driven wind successfully being launched with strong gas-dust coupling and structure formation in the form of elongated filaments on large-scales. At $t \sim 0$, the fluid is vertically stratified as per our initial conditions. The RDIs have growth times that are short relative to the flow time, with the largest scale modes

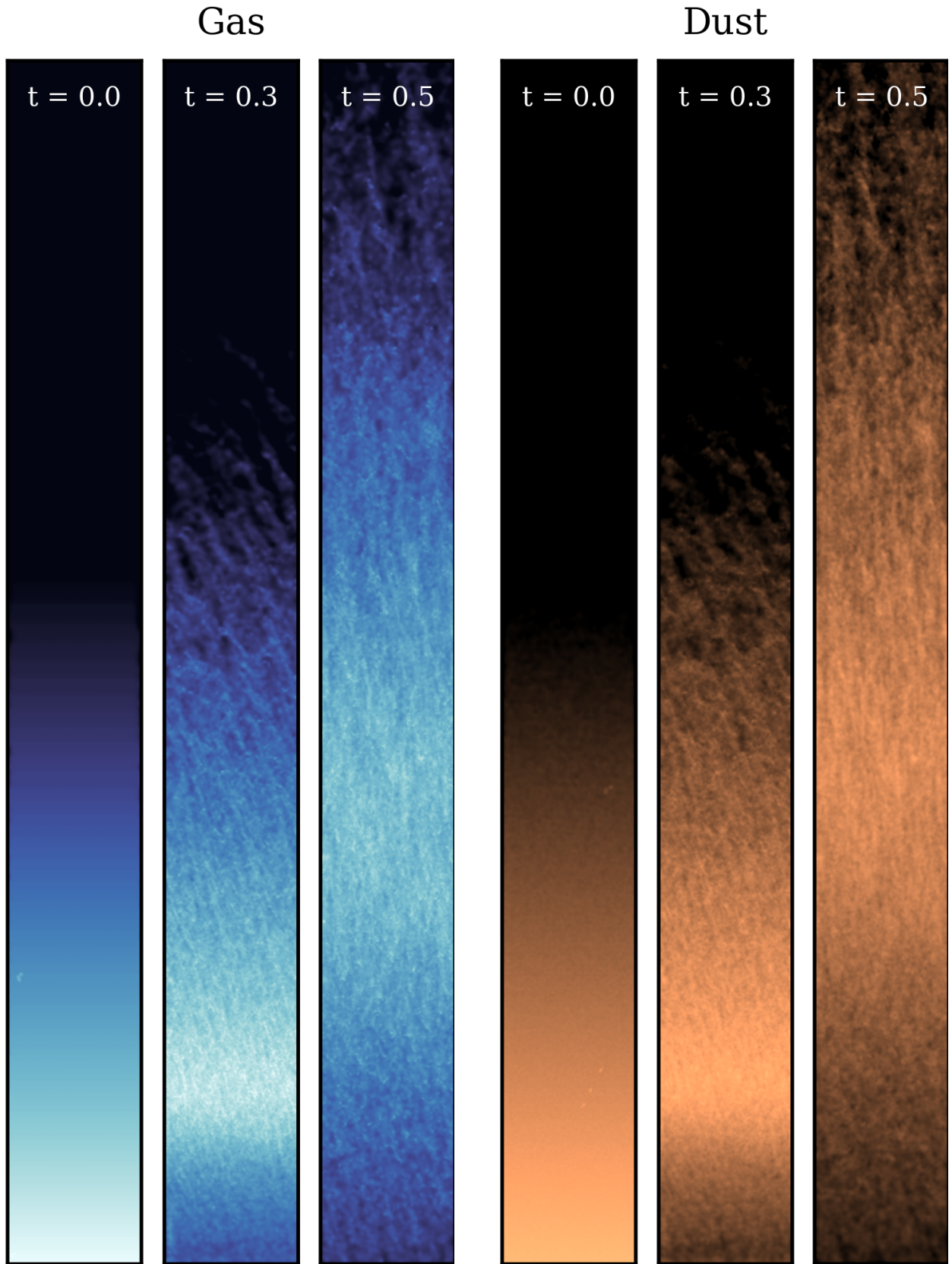


Figure 2. The evolution of the gas (right), and dust (left) column density for a simulation box with $N_{\text{H}} \sim 10^{24} \text{ cm}^{-2}$ and $\epsilon_{\text{grain}} \sim 1 \mu\text{m}$ in the x - z plane within $z \sim 0 - 9 H_{\text{gas}}$ at $t \sim (0.0, 0.3, 0.5) t_{\text{acc}}$, where t_{acc} corresponds to the acceleration timescale defined as $t_{\text{acc}} \equiv (20 H_{\text{gas}} / \langle a_{\text{eff}} \rangle)^{1/2}$ with $\langle a_{\text{eff}} \rangle \equiv \langle M_{\text{dust}} \langle a_{\text{dust, rad}} \rangle / M_{\text{total}} \rangle - g$, when a perfectly coupled fluid would have reached a height $z \sim 10 H_{\text{gas}}$. All simulations within our set show winds that were successfully launched with high degrees of clumping on small spatial scales and vertical filaments on large scales. The RDIs develop within a fraction of wind acceleration time ($t_{\text{grow}} \sim 10^{-1} t_{\text{acc}}$) with similar structure for the gas and dust. The filaments that form are initially inclined with respect to the \hat{z} -direction and align along the \hat{z} -axis at later times ($t \sim 0.5 t_{\text{acc}}$).

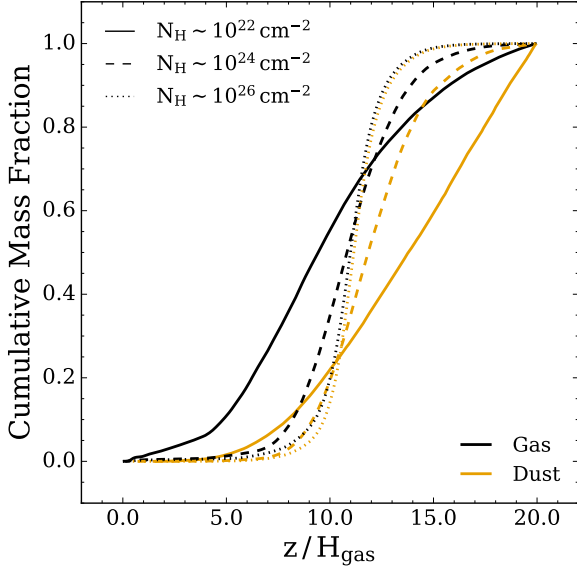


Figure 3. Cumulative mass fraction (CMF) profile of the gas (black) and the dust (yellow) for a column with maximum grain-size $\epsilon_{\text{grain}}^{\text{max}} \sim 0.1 \mu\text{m}$, and an average column density $N_{\text{H}} \sim 10^{22} \text{cm}^{-2}$ (solid line), $N_{\text{H}} \sim 10^{24} \text{cm}^{-2}$ (dashed line), $N_{\text{H}} \sim 10^{26} \text{cm}^{-2}$ (dotted line) at $t \sim t_{\text{acc}}$. At a given column density, the dust and gas show a similar profile, however, the fluid is not perfectly coupled with the gas “lagging” behind the dust. The fluid becomes more closely coupled at higher column densities as $\ell_{\text{stream, dust}} \propto N_{\text{H}}^{-1}$.

growing at a fraction ($\sim 10^{-1}$) of wind acceleration time. While the instabilities are within the linear regime, the gas and negatively charged dust develop density perturbations in the form of sinusoidal waves at an inclination angle $\sim -\theta_B^0$ from the vertical axis. As the instabilities evolve non-linearly, the inclined filaments begin aligning with the vertical axis forming elongated structures that continue to accelerate upwards.

The center of the wind, which we define as the region containing a dominant fraction of the dust (60% by mass of the dust within the central region with 20% below and above the region), reaches a height similar to that expected for a perfectly coupled homogeneous fluid without any RDIs present. However, we find that only $\sim 50\%$ of the gas remains within such heights, with roughly 40% of the gas “lagging” behind the wind. This suggests that while there exists strong micro-scale coupling between the dust and the gas through drag forces, the overall fluid is not perfectly coupled resulting in a significant fraction of the dust “leading” in-front of the gas.

Additionally, we find that the mass fraction profile of the outflow is strongly dependent on the parameters we explore within our simulation set. Figure 3 shows the cumulative mass fraction (CMF) profile of the gas and dust at $t \sim t_{\text{acc}}$ for simulations with maximum grain-size $\epsilon_{\text{grain}}^{\text{max}} \sim 0.1 \mu\text{m}$, and average column density $N_{\text{H}} \sim 10^{24} \text{cm}^{-2}$, $N_{\text{H}} \sim 10^{24} \text{cm}^{-2}$, and $N_{\text{H}} \sim 10^{26} \text{cm}^{-2}$. Both the dust and gas show a similar profile, however, the fluid is not perfectly coupled with the gas “lagging” behind the dust. We note that the separation between the gas and dust increases with increasing grain-size and decreasing density as predicted in Equation 8. In our runs with higher column densities ($N_{\text{H}} \sim 10^{25} - 10^{26} \text{cm}^{-2}$), the two plots roughly overlap as the fluid becomes closer to a perfectly coupled fluid on large scales.

3.5 Effects of Full RDMHD

In Figures 2 & 4, we compare the morphology of the simulations for our full RDMHD runs² (Fig. 4) versus the approximate “homogeneous flux” ($F_0 = \text{constant}$) simulations (Fig. 2). From left to right in Figure 4, the simulations correspond to columns with $N_{\text{H}} \sim 10^{22} \text{cm}^{-2}$, 10^{24}cm^{-2} , 10^{26}cm^{-2} respectively and $\epsilon_{\text{grain}}^{\text{max}} \sim 1 \mu\text{m}$ at $t \sim 0.5 t_{\text{acc}}$. We discuss the different regimes shown in this figure in the subsections below.

3.5.1 Intermediate Optical Depths & The “Acceleration limited” Regime

For this regime, we consider the left and middle panels in Figure 4 with $N_{\text{H}} \sim 10^{22} \text{cm}^{-2}$ and $N_{\text{H}} \sim 10^{24} \text{cm}^{-2}$, which correspond to $\tau_{\text{geo}} \sim 20$ and $\tau_{\text{geo}} \sim 2000$ respectively. With reference to Figure 2, we can see that to first order, the large-scale morphology of the RDIs does not show any significant changes when the simulations are run with our full radiative transfer treatment versus simply assuming a homogeneous radiation field. We do note the formation of a thin high density “slab” at the base of the box in the middle panel of Figure 4. This “slab” acts as an opaque wall that gets lifted by the incident photons, and effectively translates the wind upwards without significant distortions to its morphology. Nonetheless, this “slab” does not significantly affect integrated surface density along the line-of-sight or any of the macro-scale properties of the column above it such as the CMF or clumping factor profile. Therefore, we conclude that using the homogeneous radiation approximation is sufficient within this regime. We show below that the key is that the radiation diffusion time is still fast compared to timescales like the wind launch and instability growth timescales, so the radiation field is smooth.

3.5.2 Extremely Large Optical Depths: The Radiation-Propagation Limited Regime

For this regime, we consider the panel on the right in Figure 4 with $N_{\text{H}} \sim 10^{26} \text{cm}^{-2}$, which corresponds to $\tau_{\text{geo}} \sim 2 \times 10^5$. We point out that the plot shows less small-scale structure than the panels on the right due to the reduced resolution of the simulation (as noted above, this owes to using no “reduced speed of light” here, which imposes a steep computational cost penalty). As shown in the plot, accounting for full radiative transfer results in a different large-scale morphology within the box. This difference arises as the assumption of an infinitesimally small photon diffusion timescale (constant flux field) begins to break down as the photons “lag” behind the wind due to propagation effects. To determine when this occurs, we consider the ratio of the photon diffusion time, t_{diff} , to the dust acceleration time. For simplicity, we ignore the effects of gravity, and assume a homogeneous dust-gas distribution. Therefore, the ratio of the time needed for a photon to diffuse through a distance H_{γ} (the “width” of the gas “shell”) to the time required to accelerate the same “shell” to a height of $10 H_{\text{gas}}$ has the following scaling,

² In these simulations, we can optionally employ a reduced speed of light (RSOL) (see Hopkins et al. 2022), $\tilde{c} < c$. In tests, we find identical results for $\tilde{c} \sim (0.1 - 1)c$ at $N_{\text{H}} \lesssim 10^{25} \text{cm}^{-2}$, so we use $\tilde{c} = 0.1c$ here so we can run at our higher fiducial resolution. For $N_{\text{H}} \gtrsim 10^{25} \text{cm}^{-2}$, however, finite speed of light effects are important so we use $\tilde{c} = c$ (no RSOL). This imposes a large CPU cost (shorter timesteps), so the full RDMHD simulations of $N_{\text{H}} \gtrsim 10^{25} \text{cm}^{-2}$ use 10x fewer resolution elements.

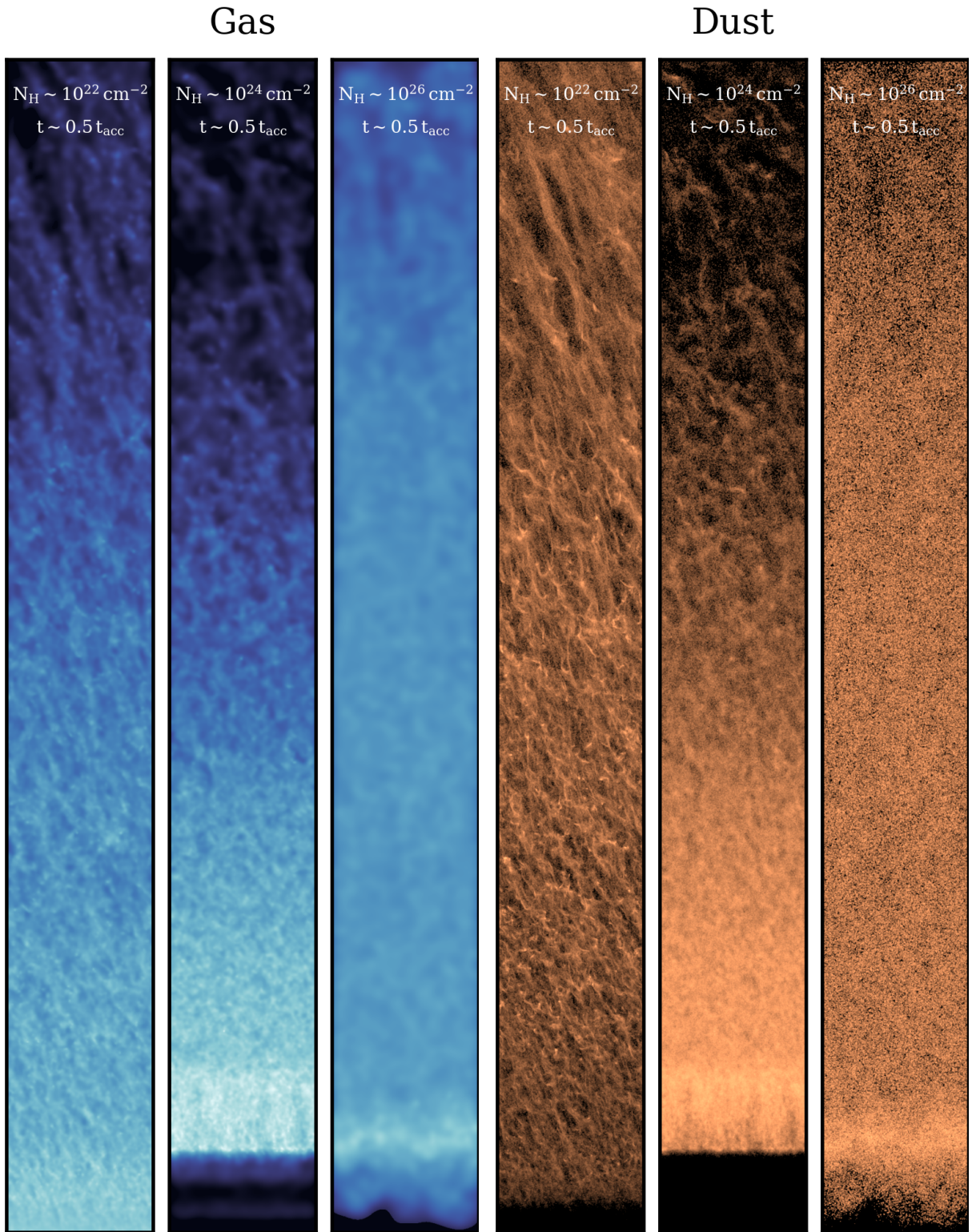


Figure 4. The gas (left) and dust (right) column densities for full RDMHD runs projected onto the x - z plane within $z \sim 1 - 9H_{\text{gas}}$ at $t \sim 0.5 t_{\text{acc}}$. From left to right, the simulations correspond to runs with $\epsilon_{\text{grain}}^{\text{max}} \sim 1 \mu\text{m}$, and $\tilde{c} \sim (0.1, 0.1, 1) c$, $N_{\text{H}} \sim 10^{22} \text{cm}^{-2}$, 10^{24}cm^{-2} , 10^{26}cm^{-2} corresponding to $\tau_{\text{geo}} \sim 20, 2000, 2 \times 10^5$ respectively. Note that the right-most plot shows less small-scale structure due to a factor of 10 reduction in resolution (owing to the cost of using $\tilde{c} = c$). For the $N_{\text{H}} \sim 10^{22} \text{cm}^{-2}$ and 10^{24}cm^{-2} , the optical depth is sufficiently low such that full treatment of RDMHD shows similar structure formation on small and large scales to the runs without explicit radiative transfer. For the $N_{\text{H}} \sim 10^{26} \text{cm}^{-2}$ column, the high optical depth results in photon diffusion time that are longer than the wind acceleration time expected from a constant flux assumption resulting in a slower outflow.

$$\frac{t_{\text{diff}}}{t_{\text{acc}}} = \frac{H_{\gamma}^2 \mu^{\text{dg}} \rho_g \kappa a_{\text{eff}}^{1/2}}{\sqrt{20H_{\text{gas}}c}} \quad (12)$$

$$= \frac{3}{8\sqrt{5}} \frac{c_s}{c} \langle Q_{\text{ext}} \rangle \tilde{a}_d^{1/2} \left(\frac{\mu^{\text{dg}}}{\tilde{\alpha}_m} \right)^{3/2} \left(\frac{H_{\gamma}}{H_{\text{gas}}} \right)^2 \quad (13)$$

$$\sim 5 \times 10^4 \left(\frac{c_s/c}{10^{-5}} \right) \left(\frac{\langle Q_{\text{ext}} \rangle}{1} \right) \left(\frac{\tilde{a}_d}{5 \times 10^7} \right)^{1/2} \left(\frac{\tau_{\text{geo}}}{20000} \right)^{3/2} \left(\frac{H_{\gamma}}{H_{\text{gas}}} \right)^2 \quad (14)$$

where κ is the dust opacity, $\tilde{a}_d \equiv (3/4) (F_0 \langle Q \rangle_{\text{ext}} / c) / (\rho_{\text{base}} c_s^2)$ is the dimensionless dust acceleration parameter, and we assume that $c_s/c \sim 10^{-5}$ ($T_{\text{gas}} \sim 1000$ K), matching the assumptions used in our simulations. In addition, for simplicity we assume that the grains all have the median grain-size ($\epsilon_{\text{grain}} \sim 0.1 \epsilon_{\text{grain}}^{\text{max}}$) and not a grain-size spectrum. It is important to note that the expression above is sensitive to the value of τ_{geo} . When comparing our lowest optical depth simulation ($N_{\text{H}} \sim 10^{22} \text{ cm}^{-2}$) to our highest ($N_{\text{H}} \sim 10^{26} \text{ cm}^{-2}$), there is an increase of a factor of 10^4 in τ_{geo} , which in turn results in a factor of 10^6 in the ratio of the two timescales considered above. Therefore, in the higher optical depth case case, the radiation can no longer propagate fast enough to reach the material at the top of the box to maintain a constant flux. Consequently, material at the “top” of the box in the ICs can fall down before radiation reaches it and the outflow propagation speed is limited not just by naive total acceleration but also photon transport time, resulting in a wind with a slower outflow velocity. However, despite the morphological change on large-scales, this effect mostly acts to reduce the vertical translation of material in the column at a given time, and has minimal effect on the internal properties of the outflow.

3.6 Do Winds Launch?

As shown in Figures 2 and 3, our plots indicate that the accelerated dust imparts sufficient momentum onto the gas to successfully launch a wind across our entire parameter survey. As photons propagate through the box, they could in principle escape through low density “channels”, and thus, impart lower amounts of their momentum onto the dust resulting in $p^{\text{total}} < \int \tau L/c dt$. We show the gas and dust components of the total momentum (note that we multiply the dust momentum by a factor of $1/\mu^{\text{dg}} = 100$ for ease of comparison) in the wind relative to the predicted momentum $\int \tau L/c dt$ in Figure 5. The plots show that prior to the growth time for the instabilities, $t \lesssim 0.1 t_{\text{acc}}$, the radiation is well coupled to the fluid. However, as the instabilities grow, the line for the expected momentum of $\int \tau L/c dt$ begins to separate from the imparted momentum as low density “channels” develop. At $t \sim t_{\text{acc}}$, the plots show factors 1–3 of momentum “leakage” from the box which increases with increasing column density. We attribute this effect to slower photon diffusion at higher column densities which results in an overall reduced incident flux on the dust particles. But we still always see an order-unity fraction of the radiation momentum $\int \tau L/c dt$ actually couples, and thus is always sufficient to launch a wind under AGN-like conditions as simulated here.

In addition, we also study the behavior of the wind in an environment where gravity dominates over the radiation-driven acceleration, i.e. where $\tau L/c \lesssim g M_{\text{gas}}$, or in our dimensionless units $\tilde{\alpha}/\tilde{g} \lesssim 1$ (though we note we are only modestly in this regime here, with gravity

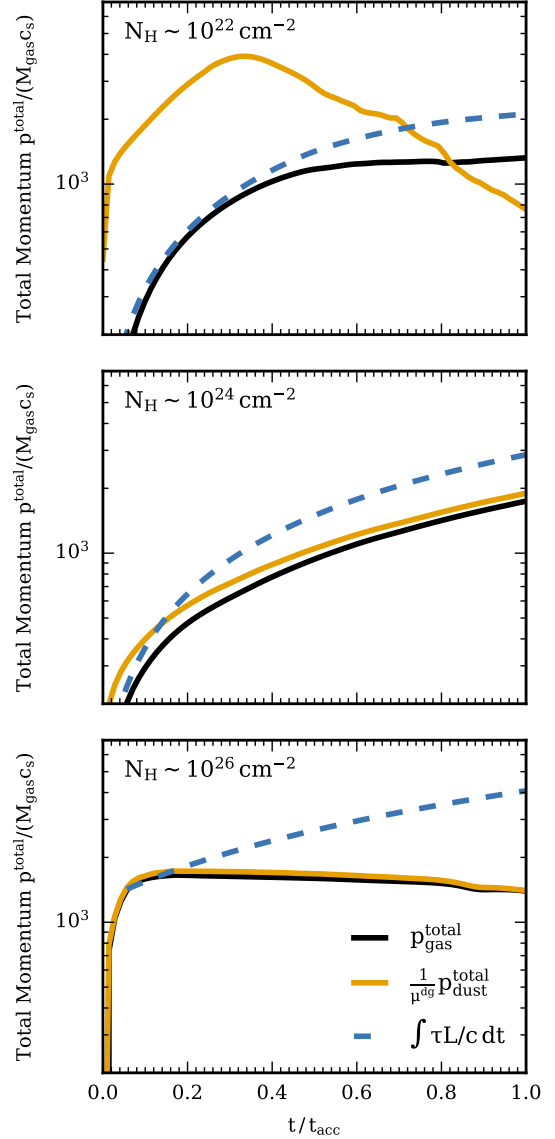


Figure 5. Gas (black) and dust (yellow) total momentum normalized to the product of the total gas mass within the box at $t = 0$ and the speed of sound compared to expected momentum in the wind (blue dotted line) in the homogeneous perfect-coupling gray opacity limit, $p^{\text{total}} \sim \int t \tau L/c dt$ for 3 RDMHD runs. Note that we multiply the dust momentum by a factor of $1/\mu^{\text{dg}} = 100$ for plotting purposes. From top to bottom, the total gas column density N_{gas} corresponds to 10^{22} cm^{-2} , 10^{24} cm^{-2} , and 10^{26} cm^{-2} respectively, and maximum grain-size of $1 \mu\text{m}$. The plots show factors of 1–3 momentum “leakage”, with higher leakage for denser columns. The top panel shows a turnover in the dust momentum as most energetic dust particles escape from the box.

a factor of ~ 3 stronger than radiation). We show the projected morphology of the gas column under these conditions evolved to $t \sim (0.7, 1.0, 1.3, 1.7) t_{\text{acc}}$ in Figure 6. As the net vertical acceleration is in the negative z direction, we define the acceleration time as $t_{\text{acc}} = \sqrt{20H_{\text{gas}}/|a_{\text{eff}}|}$ for this simulation. The simulation is run with full RDMHD with the following parameters: $\tilde{c} \sim 0.1 c$, $N_{\text{H}} \sim 10^{24} \text{ cm}^{-2}$ and $\epsilon_{\text{grain}}^{\text{max}} \sim 0.01 \mu\text{m}$. Naively, we would expect a failed wind to result from these conditions, however, as shown in the plots, much of the gas (and dust as they are tightly coupled in this simulation), is

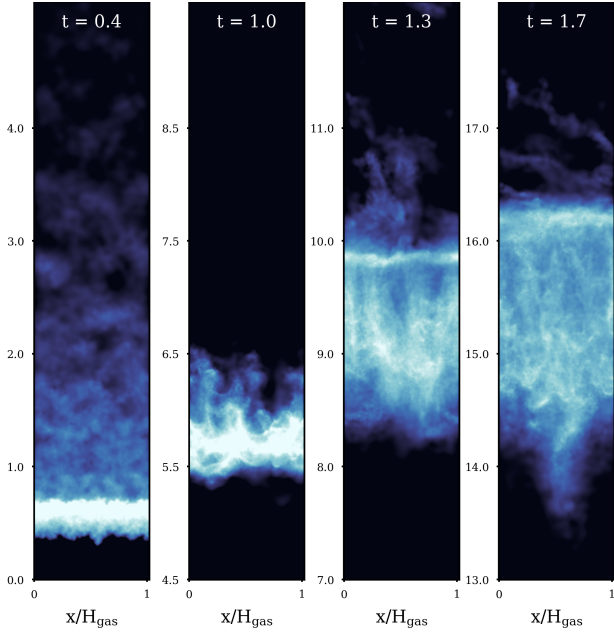


Figure 6. The evolution of the gas column density for an RDMHD simulation box with $\tilde{c} \sim 0.1c$, $N_H \sim 10^{24} \text{cm}^{-2}$ and $\epsilon_{\text{grain}}^{\text{max}} \sim 0.01 \mu\text{m}$ in the x - z plane at $t \sim (0.7, 1.0, 1.3, 1.7) t_{\text{acc}}$, where for this case $t_{\text{acc}} = \sqrt{20H_{\text{gas}}/|a_{\text{eff}}|}$. For this simulation, we initialize the box such that in the perfect dust-to-gas coupling limit, the net force from gravity is stronger than the radiation pressure force by a factor of ~ 3 . The plot shows that despite the strength of gravity being stronger than the radiation driven acceleration, a non-negligible component of the dust and gas is still ejected, however, the resulting ejecta is more compressed relative to our default setup, and a somewhat larger fraction “falls back”.

successfully ejected. The increased strength of gravity does not cause the wind to halt, but rather compresses the gas and dust to a more compact “shell”. After the ejecta is compressed to a thin slab, the radiation continues to accelerate the material, resulting in a thicker slab with prominent substructure at later times. Some gas indeed “falls back” - more than in our fiducial simulations with $\tilde{g} < \tilde{\alpha}$; but the same in-homogeneity that allows tens of percent of gas to “fall down” in those simulations leads to tens of percent gas ejected here.

3.7 Gas and Dust Clumping and Coupling in AGN Winds

As discussed above, we find that the dust and gas within the fluid are not always perfectly coupled. In Figure 7, we quantify this by computing the gas-gas, dust-dust, and dust-gas clumping factors defined in Equation 16, as a function of height within the simulation box at $t \sim \min(t_{\text{acc}}, t_{\text{esc}})$.

$$C_{nm} \equiv \frac{\langle \rho_n \rho_m \rangle_V}{\langle \rho_n \rangle_V \langle \rho_m \rangle_V} \quad (15)$$

$$= \frac{V \int_V \rho_n(\mathbf{x}) \rho_m(\mathbf{x}) d^3\mathbf{x}}{\left[\int_V \rho_n(\mathbf{x}) d^3\mathbf{x} \right] \left[\int_V \rho_m(\mathbf{x}) d^3\mathbf{x} \right]} = \frac{\langle \rho_n \rangle M_m}{\langle \rho_n \rangle V} \quad (16)$$

As shown in the equation, the clumping factor is analogous to the auto-correlation (for like species) and the cross-correlation (for different species) function of the local density field, where factors less than 1 imply an anti-correlation. We report clumping factors $\sim 1 - 10$

for the gas-gas and dust-dust clumping factors, and ~ 1 for dust-gas clumping. The gas-gas clumping factors, C_{gg} , are lower at the base of the wind, and increase up to a roughly constant value within the accelerated wind. As the gas is collisional and pressurized, its clumping is limited by pressure forces, especially on small spatial scales inside the wind. We note that for the run with $N_H \sim 10^{22}$, $\epsilon_{\text{grain}}^{\text{max}} \sim 1 \mu\text{m}$, the gas has high clumping factors at $z \sim 10 \rightarrow 20 H_{\text{gas}}$. This occurs as for this parameter space, due to the low gas column density and high acceleration forces, which make the gas effectively more compressible.

The dust-dust clumping factors, C_{dd} , show a constant rise as a function of height to reach maximal values at the top of the box, and the slope of the profile weakly increases with grain-size and weakly decreases with density. If we assume that C_{dd} is purely driven by the saturation of the of the RDIs, we expect clumping at some height z to be stronger where the RDI growth-time at a given wavelength is shorter. Plugging in equilibrium values of w_s and t_s in the supersonic limit into Equation 4, we obtain

$$t_{\text{grow}}(\lambda, z) \sim \left(\frac{\lambda^4 \rho_g e^{-z/H_{\text{gas}}} c_s^3}{a_{\text{eff}} \bar{\rho}_{\text{grain}}^i \epsilon_{\text{grain}} (\mu^{\text{dg}})^5} \right)^{1/6} \quad (17)$$

$$\propto \rho_g e^{-z/6H_{\text{gas}}}. \quad (18)$$

As all the parameters in the expression above with the exception of the stratified density term are roughly independent of height, we expect the RDI growth-timescale to get shorter as a function of height. In turn, the degree of dust clumping would increase as a function of height (clumping is ~ 5 times stronger for a factor ~ 10 increase in height) as shown in our plots. We note that this effect is suppressed for some of our simulations which could arise due to the non-linear evolution of the RDI's and/or competing processes such as turbulence.

In Figure 8 we plot the zoomed-in column density profiles of the gas (left) and dust (right) in several RDMHD simulations. From top to bottom, the maximum grain-size $\epsilon_{\text{grain}}^{\text{max}}$ corresponds to $0.01 \mu\text{m}$, $0.1 \mu\text{m}$, and $1 \mu\text{m}$ respectively, for an average column density of 10^{22}cm^{-2} within the simulation box. The structures formed appear more diffuse for smaller grain-sizes. Usually, we see sharper structures for lower τ_{geo} , which could be shown by considering how t_{grow} depends on τ_{geo} . In Equation 11, we showed that $t_{\text{acc}}/t_{\text{grow}} \propto \tau_{\text{geo}}^{-1/6}$, therefore environments with lower τ_{geo} would result in sharper structure.

As the micro-scale structure of the dust within the torus is not spatially-resolved observationally, we cannot directly compare the structures formed within our simulations to observations. Nonetheless, the physical variation in column densities could be inferred from the time variability for AGN sources. We discuss this in further detail in Subsection 3.9.

3.8 Evolution of Velocity Fluctuations

To further analyze the evolution of the resultant non-uniform internal structure of the outflows within our simulations, we explore velocity fluctuations in dust and gas here. It is important to note that there are multiple RDI modes present simultaneously within the simulation

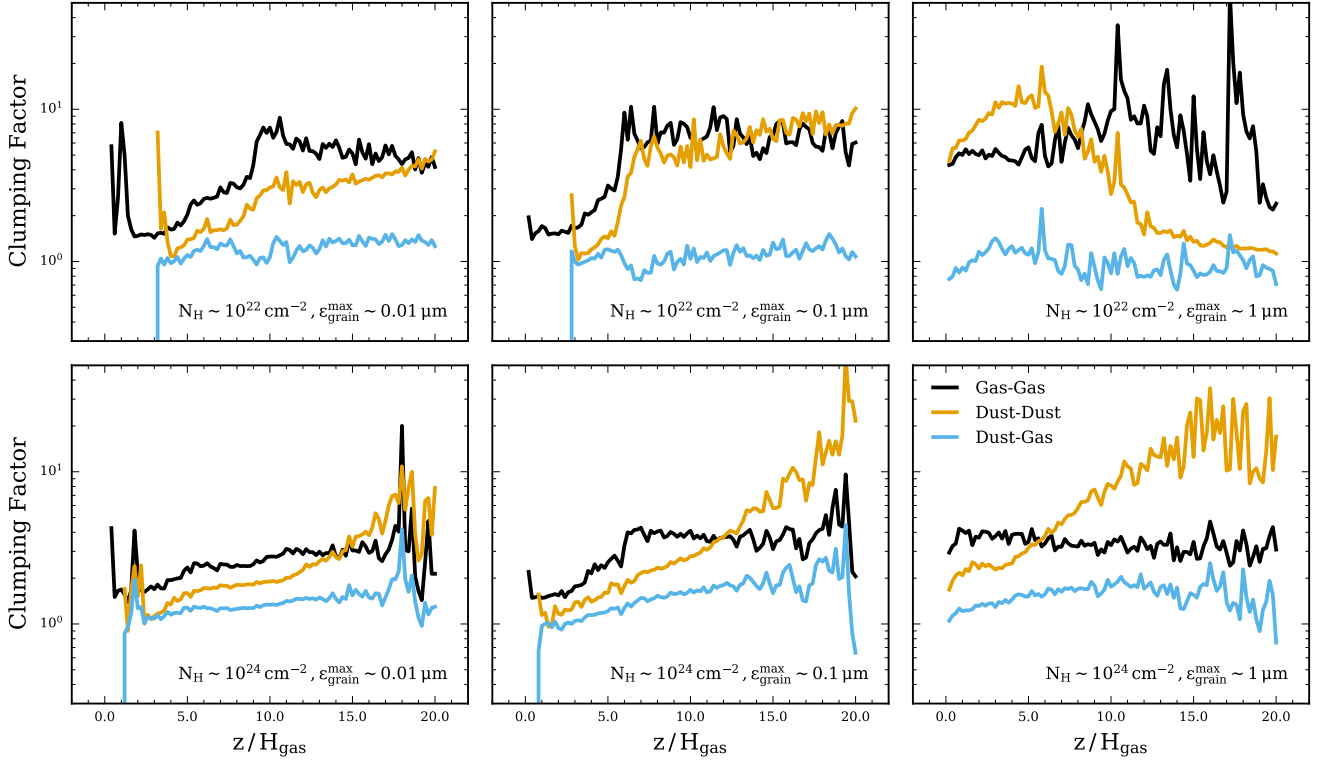


Figure 7. Clumping factors for gas-gas ($\langle \rho_g^2 \rangle / \langle \rho_g \rangle^2$), dust-dust ($\langle \rho_d^2 \rangle / \langle \rho_d \rangle^2$), and gas-dust ($\langle \rho_g \rho_d \rangle / \langle \rho_g \rangle \langle \rho_d \rangle$). From left to right, the maximum grain-size $\epsilon_{\text{grain}}^{\text{max}}$ corresponds to $0.01 \mu\text{m}$, $0.1 \mu\text{m}$, and $1 \mu\text{m}$ respectively, for an average column density of 10^{22}cm^{-2} (top) and 10^{24}cm^{-2} (bottom) within the simulation box. Gas-gas, dust-dust and gas-dust clumping is significant near the center of the wind where most of the mass resides. Further, dust-dust and gas-dust clumping is stronger for larger grains. For an extended discussion, refer to §3.7.

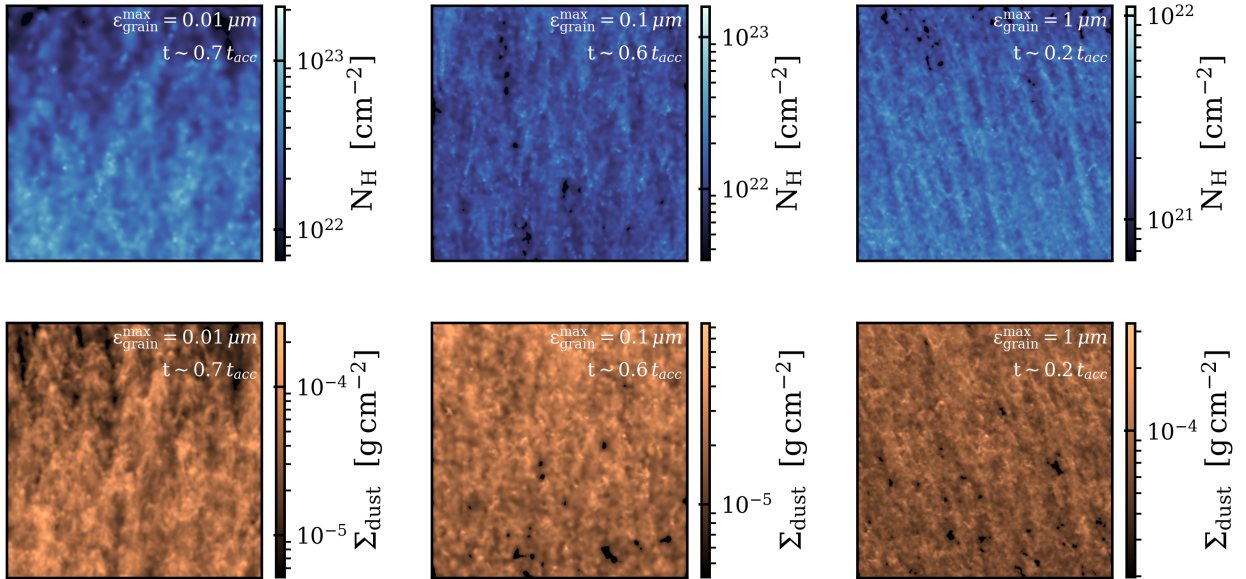


Figure 8. Gas column density (top) and dust surface density (bottom) within narrow bins in a zoomed-in region of high density within the AGN wind projected along the x - z plane at $t \sim t_{\text{esc}}$ (where t_{esc} is the time at which 10% of the dust/gas has escaped the top of the box). From left to right, the maximum grain-size $\epsilon_{\text{grain}}^{\text{max}}$ in the simulation box corresponds to $0.01 \mu\text{m}$, $0.1 \mu\text{m}$, and $1 \mu\text{m}$ respectively, for an average column density of 10^{22}cm^{-2} at times 0.7 , 0.6 and $0.2 t_{\text{acc}}$. Note that as the absorption efficiency is grain-size dependent, the dust surface density is proportional to the extinction with $A_\lambda \sim 0.1 (\Sigma / 10^{-4} \text{g cm}^{-2}) (\mu\text{m} / \epsilon_{\text{grain}}^{\text{max}})$. Larger grains show stronger clumping and thus more defined filaments.

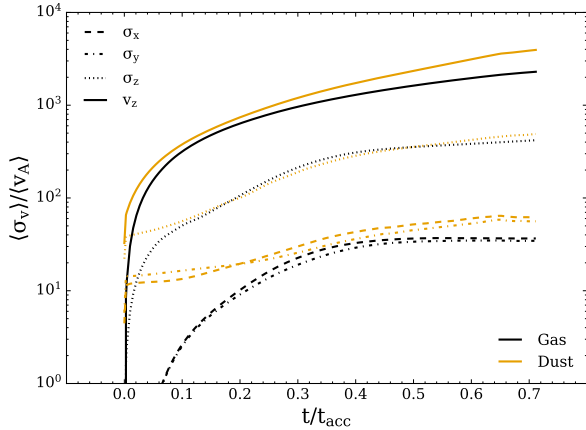


Figure 9. The temporal profile of the gas (black) and dust (yellow) random velocity dispersion (RMS) and outflow velocity relative to the box averaged Alfvén speed, for a simulation box with $N_{\text{H}} \sim 10^{24}$, $\epsilon_{\text{grain}}^{\text{max}} \sim 1\mu\text{m}$. The RMS random velocity dispersion quickly saturates in all directions for both the gas and the dust. The RMS dispersion is dominated by the z-component ($\sim 10\%$ variation), i.e. the direction of the outflow, due to slightly different drift speeds for the gas, different dust sizes and different sub-structures. The x and y components are ~ 1 order of magnitude weaker.

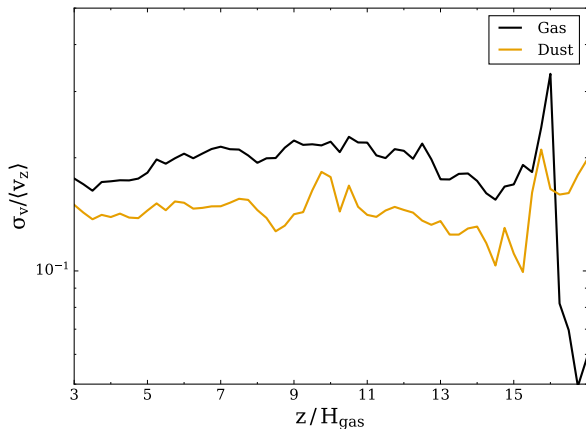


Figure 10. The spatial profile of the gas and dust random velocity dispersion (RMS) in the z-direction normalized to the average outflow velocity, v_z at a given height z , for a simulation box with $N_{\text{H}} \sim 10^{24} \text{cm}^{-2}$, $\epsilon_{\text{grain}}^{\text{max}} \sim 1\mu\text{m}$ at $t \sim 0.7 t_{\text{acc}}$. The plot shows that the ratio of σ_z/v_z , remains roughly constant as a function of height along the box. We only show the z-component in this plot as the x and y components show a similar behavior but a magnitude weaker in the ratio of their respective velocity dispersion to the outflow velocity.

box, and while the short wavelength modes will have the shortest growth times (Hopkins & Squire 2018b), the dynamics will be dominated by the large-scale modes, as well as non-linear effects and in-homogeneity in the wind (eg. different clumps/ filaments moving differently).

Figures 9 and 10 show the evolution of the box averaged root mean squared (RMS) (x, y, z and 3D components) random velocity dispersion, σ_v , relative to the Alfvén speed of the dust and gas relative to the wind acceleration time t_{acc} , and the RMS σ_{vz} relative to the mean velocity in the z-direction at a given height, as a function of height z respectively. The plot shows the behavior for

our $N_{\text{H}} \sim 10^{24} \text{cm}^{-2}$, $\epsilon_{\text{grain}}^{\text{max}} \sim 1\mu\text{m}$ run, however, we note that we observe the same behavior throughout our parameter space. The dispersions grow exponentially fast (as expected if they are RDI-driven) at early stages and quickly saturate (within $0.1-0.2 t_{\text{acc}}$) for all runs within our parameter set. This suggests that in an AGN torii, such instabilities have already saturated within the time taken to launch a wind, and later structure formation is mostly driven by radiation-pressure accelerating the medium in addition to the turbulence within the flow.

Further, at the non-linear stage of their evolution, the gas and dust both reach similar super-Alfvénic random velocities with the RMS dispersion dominated by the z-component. The x and y components are ~ 1 order of magnitude weaker due to the inherent geometry of the problem and the relatively weak Lorentz forces.

Analysing the spatial profile, we note $\sim 20\%$ and $\sim 2\%$ dispersion in the z and x-y directions respectively relative to the outflow velocity. Towards the base ($z \sim 0-3$), and top ($z \sim 17-20$) of the wind, the profile shows anomalous behavior due to the presence of a relatively low number of dust particles/gas cells and boundary effects. Away from the boundaries, the dispersion shows no spatial dependence.

3.9 Temporal and Spatial Variability in Column Densities along Observed Sightlines

While it is difficult to resolve the underlying structure of the dust within AGN torii, AGN spectra and SEDs with high temporal resolution can be obtained which could probe these small-scale fluctuations. The methodology here closely follow Steinwandel et al. (2021) to which we refer for details. In Figure 11, we therefore compute the time variability in the sight-line integrated surface density of the dust and gas integrated for an infinitesimally narrow line-of-sight down the z-direction i.e. towards the accretion disk which should have an angular size that is very small compared to our resolution (hence an effectively infinitesimally narrow sightline), and show the variance of the distribution in Figure 12. From top to bottom, the total gas column density N_{H} in the simulation box corresponds to 10^{22}cm^{-2} , 10^{24}cm^{-2} , and 10^{26}cm^{-2} respectively, and maximum grain-size is $0.01\mu\text{m}$ (left), and $1\mu\text{m}$ (right). The plots show variability of order a few % for both the dust and gas over relatively short timescales (a few years in physical units), and up to $\sim 20-60\%$ variation on long timescales (decades). The amplitude of the short-timescale variations is roughly independent of maximum grain-size, and decreases for denser columns. This result is consistent with our findings for the underlying morphological structure of the wind, where for low column density boxes with large grains, we find that the RDIs led to the generation of defined dense vertical filaments which would cause significant variability as they cross the line-of-sight. Further, the variability extends beyond the time taken for the instabilities to grow, and is likely driven by the large dispersion velocities of the dust and gas. However, while the magnitude of the velocity dispersion is similar across all our runs, denser columns form more randomized clumps which are likely to be averaged over when integrating down the z-direction, and thus result in weaker variation in the sightline quantities compared to the 3D quantities (see e.g. Hopkins et al. 2022).

In principle, fluctuations in Σ could also exhibit corresponding fluctuations in the line-of-sight grain-size distribution, as shown for

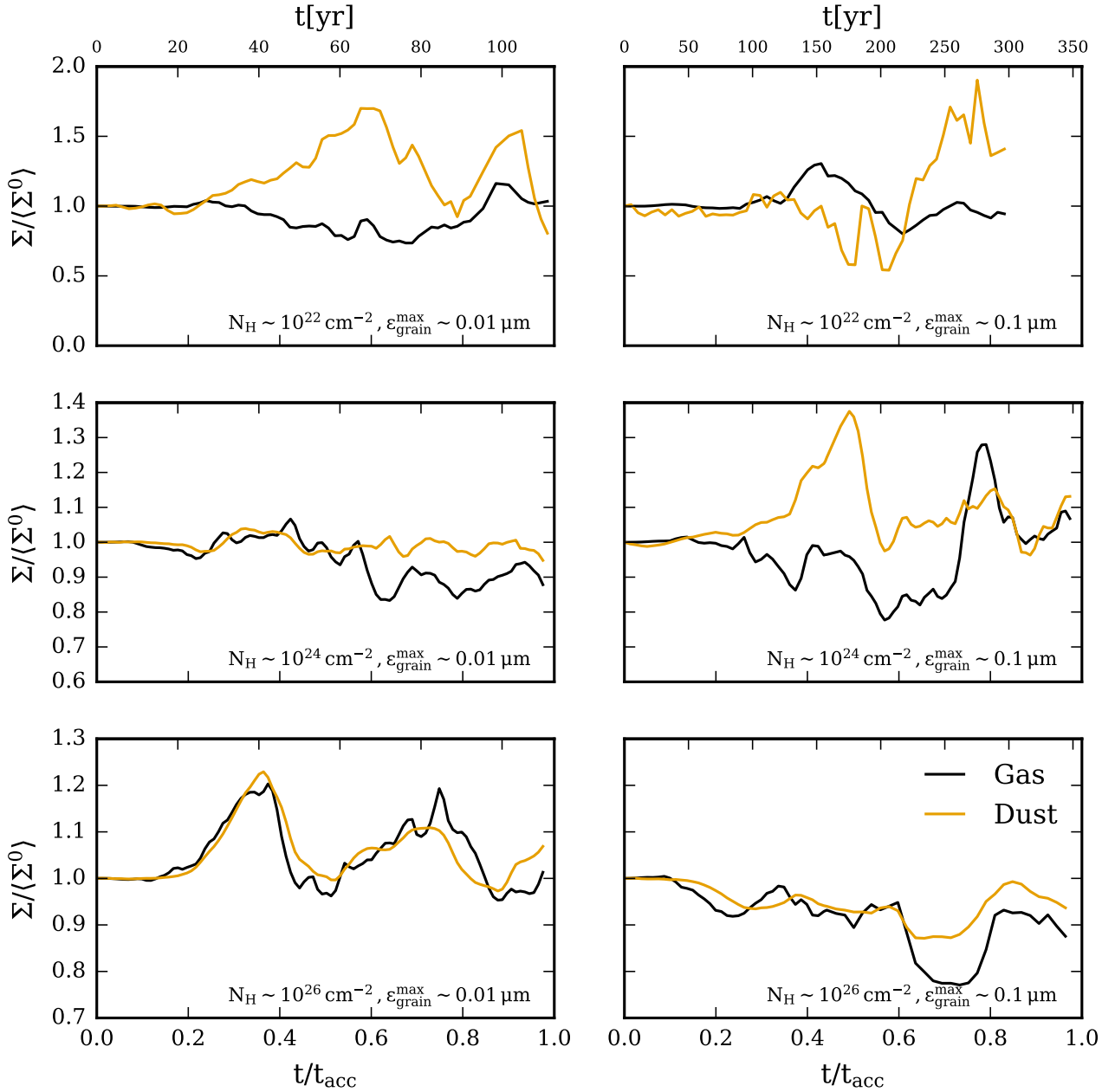


Figure 11. The sight-line integrated surface density Σ along a random line-of-sight towards the AGN accretion disk. We normalize Σ to Σ^0 , the initial mean surface density in the simulation box for convenience. We compare both gas and dust columns, from top to bottom, the total gas column density N_{H} in the simulation box corresponds to 10^{22}cm^{-2} , 10^{24}cm^{-2} , and 10^{26}cm^{-2} respectively, and maximum grain-size is $0.01\mu\text{m}$ (left), $0.1\mu\text{m}$ (right). Overall, the dust and gas show fluctuations of similar amplitude, and there is an order a few % variability on short timescales (a few years), with higher variation ($\sim 10 - 40\%$) on long timescales relative to the acceleration time of the wind. However, at a given time the gas and dust Σ fluctuations do not exactly match.

e.g. AGB-star outflows in [Steinwandel et al. \(2021\)](#). Therefore, we analyze the spatial fluctuations in the grain-size distribution in the same manner as Σ . However, we find that the fluctuations in the grain-size distribution are significantly weaker than the environments studied in [Steinwandel et al. \(2021\)](#) (perhaps consistent with our Σ fluctuations themselves being much weaker), and largely fall within the range we might expect from shot noise given our limited resolution (the shot noise being large for grain-size fluctuations since we must consider only a narrow range of grain-sizes, hence a more limited number of

dust particles). Therefore we cannot conclusively say whether or not there is a potentially-measurable correlation between the fluctuations in Σ and the grain-size distribution.

In [Figure 12](#), we show the spatial variability of the logarithmic gas and dust integrated surface densities computed over all possible sight-lines as a function of time. As one would expect, there is an increasing variation of the surface densities as the RDIs develop. For lower column densities, the dust surface density shows higher variability for larger grain-sizes. However, for the higher column

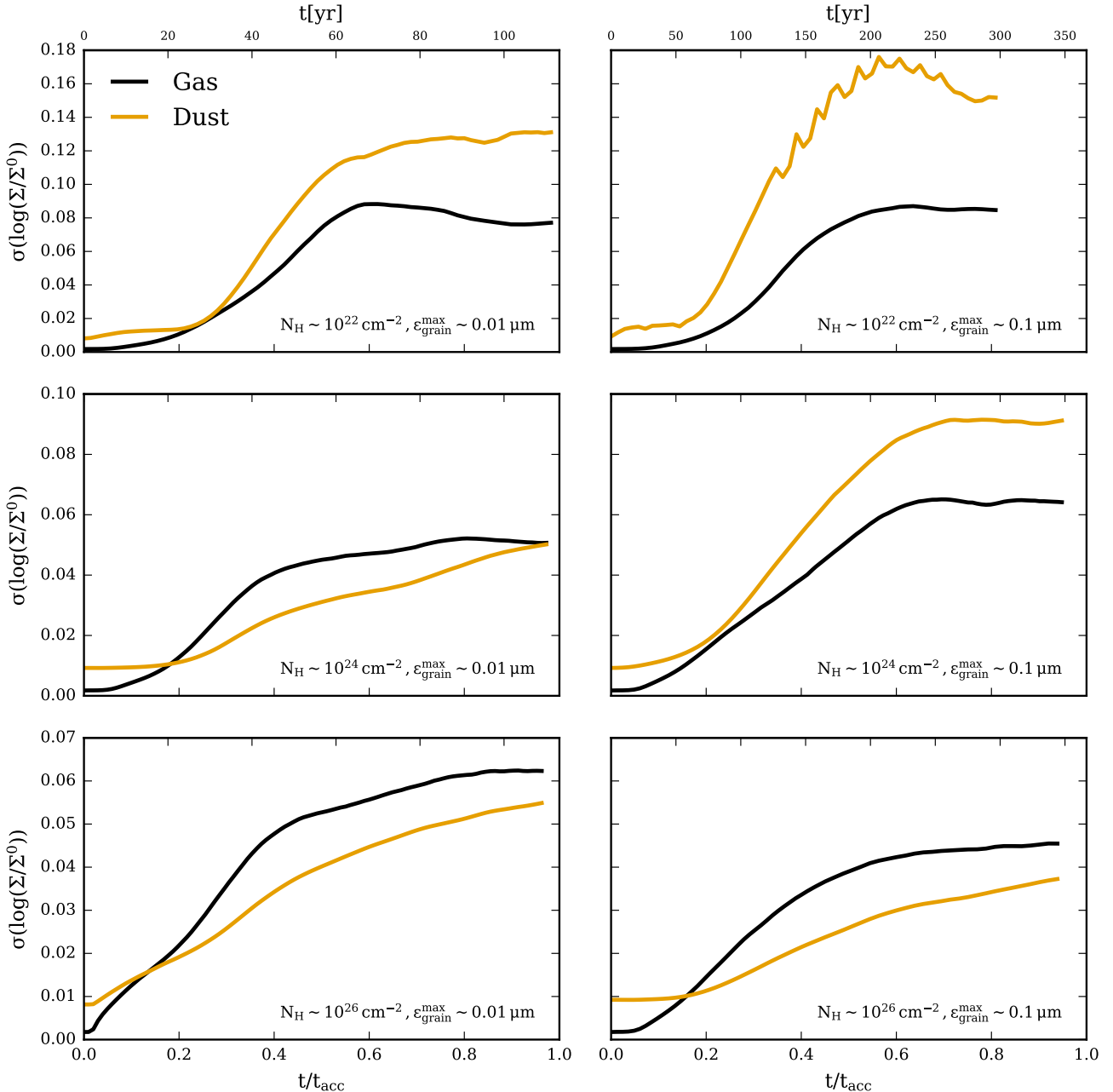


Figure 12. The sightline-to-sightline spatial variability of the gas and dust integrated surface densities across different sight-lines within the box as a function of time. We specifically plot 1σ dispersion in the log of the surface density compared across 100 random sightline to the AGN accretion disk, through the wind, at each time t . From top to bottom, the total gas column density N_{H} in the simulation box corresponds to 10^{22}cm^{-2} , 10^{25}cm^{-2} , and 10^{26}cm^{-2} respectively, and maximum grain-size is $0.01\mu\text{m}$ (left), and $1\mu\text{m}$ (right). Both the gas and the dust show similar degrees of variability, with the dust variability increasing at a higher rate at later times. We note that below $N_{\text{H}} \sim 10^{26}\text{cm}^{-2}$, larger grains result in a larger variation due to more prominent vertical filaments across the simulation, however, the grain-size has a minimal affect on the spread of the distribution for higher column densities.

density runs $N_{\text{H}} \geq 10^{22}\text{cm}^{-2}$, there is a weak dependence of the surface density variation on the grain-sizes with the dust and gas showing roughly similar variation across different maximum grain-sizes. Further, we note a trend of decreasing variation for increasing column densities.

To interpret the trend in variability, we follow the analysis presented in Moseley et al. (2019). Assuming pure isothermal MHD turbulence, the variance of the gas density field will roughly follow

a log-normal distribution of the form,

$$\sigma^2(\ln(\rho_g)) = \ln(1 + (b|\sigma_v/c_s|)^2),$$

where b corresponds to the "compressibility" of the fluid with $b \sim 0.2 - 1$. We expect the saturation amplitude of the turbulence within the box to occur when the eddy turnover timescale is of order the growth timescale of the instability mode, this results in the following scaling for the long-wavelength regime,

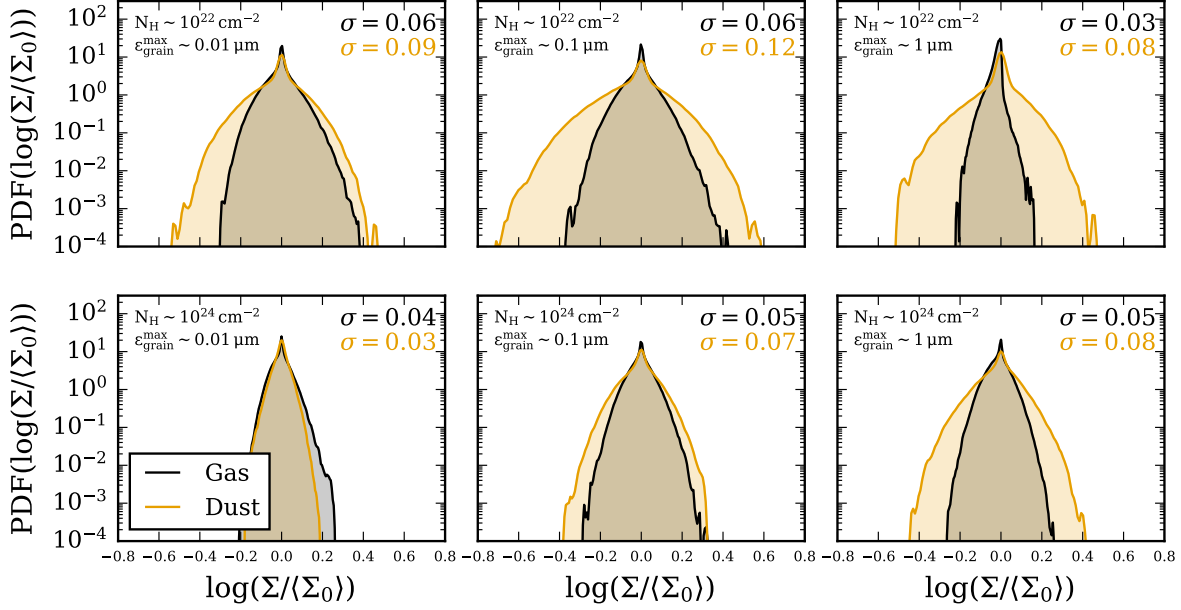


Figure 13. The normalized probability density function (PDF) of the surface density for the dust and gas components across 100 random sightlines at each time, combining all times after the wind begins to launch ($t > 0.1t_{\text{acc}}$). From top to bottom, the total gas column density N_{H} in the simulation box corresponds to 10^{22}cm^{-2} and 10^{24}cm^{-2} , and maximum grain-size is $0.01\mu\text{m}$ (left), $0.1\mu\text{m}$ (middle), $1\mu\text{m}$ (right). The PDF's show distributions that are highly non-gaussian with a narrow peaked core component and wings with steep drop offs as result of enhanced fluctuations. On average, the dust shows a higher spread in the distribution than the gas as expected given its collisionless nature. This difference in spread decreases as the fluid approaches the limit of being perfectly coupled, i.e. smaller grain-sizes, and higher column densities, again as expected for the RDI's.

$$\sigma_v \sim (\mu^{\text{dg}})^{1/3} (k \langle c_s \rangle \langle t_s \rangle)^{2/3} (\langle \mathbf{w}_s \rangle / c_s)^{2/3}.$$

Therefore, combining both relations, we get,

$$\sigma(\log(\rho_g)) \sim \ln(1 + \rho_g^{-4/3} \epsilon_{\text{grain}}^{1/3}).$$

So in the case where $\rho_g^{-4/3} \epsilon_{\text{grain}}^{1/3} \gg 1$, the variability will be higher for columns with lower density and larger grain-sizes with a strong dependence on the density and a weak dependence on the grain-size. However, when $\rho_g^{-4/3} \epsilon_{\text{grain}}^{1/3} \ll 1$, the variability will be roughly similar at all densities and grain-sizes.

In Figure 13, we show the normalized PDF of the logarithmic surface density field for all times after the saturation of the RDIs and all sight-lines. From top to bottom, the total gas column density N_{gas} in the simulation box corresponds to 10^{22}cm^{-2} and 10^{24}cm^{-2} respectively, and maximum grain-size is $0.01\mu\text{m}$ (left), $0.1\mu\text{m}$ (middle), $1\mu\text{m}$ (right). We omit the plots for larger column densities, but report that they are similar to the bottom left plot. As shown in the plots, the profile of the PDF's is highly non-gaussian with a narrow peaked core component and wings that sharply drop off, indicative of strongly enhanced fluctuations. The dust PDF is broader than that of the gas at lower column densities and higher grain-sizes, i.e. when the dust is not well-coupled with the gas. This difference in negligible for more obscured lines-of-sight ($N_{\text{H}} \gtrsim 10^{24}\text{cm}^{-2}$), as the fluid is strongly coupled across the range of grain-sizes we consider.

3.9.1 Power Spectral Analysis

In Figure 14, we show the temporal power spectrum, for individual lines-of-sight (as Fig. 2) and averaged over all lines-of-sight, of the line-of-sight integrated gas and dust surface density in black and yellow thick lines respectively. We show this for a simulation with $N_{\text{H}} \sim 10^{24}\text{cm}^{-2}$ and $\epsilon_{\text{grain}}^{\text{max}} \sim 0.01\mu\text{m}$. We omit the spectra for the remainder of our simulation set as they show a similar profile shape. The spectra for dust and gas show similar profiles, with twice the amount of power present in the dust spectrum relative to the gas (consistent with all our previous analysis). The plot indicates that, most of the power is on long timescales, with a spectral index $\alpha_v \sim -1$, defined as $dP/d \ln \nu \propto \nu^{\alpha_v}$. This spectral index is very close to canonical red noise which is consistent with AGN observations (Caplar et al. 2017; MacLeod et al. 2012), and could arise from an array of physical processes. For instance, if we assume that on small-scales, the density fluctuations take the form of a Gaussian random field, as the surface density is an integral over that field, it is natural that the resulting power spectrum would take this form. Further, we note that the plateaus at high frequencies are likely an artifact due to our limited time-resolution and simulation duration.

In Figure 15, we show the spatial power spectrum of the logarithm of the 3 dimensional density field for a column with $N_{\text{H}} \sim 10^{24}\text{cm}^{-2}$ and $\epsilon_{\text{grain}}^{\text{max}} \sim 0.01\mu\text{m}$, and similarly to above, note that it is roughly consistent with the spectra for our other simulations. The plot shows similar profiles for the dust and the gas, which is indicative that on the relatively large-scales that we are probing, the dust and gas fluctuations are order-of-magnitude comparable. Further, the power increases exponentially with a spectral index $\alpha_k \sim 1$, defined as $dP/d \ln k \propto k^{\alpha_k}$ until a few factors of the resolution limit is hit, after

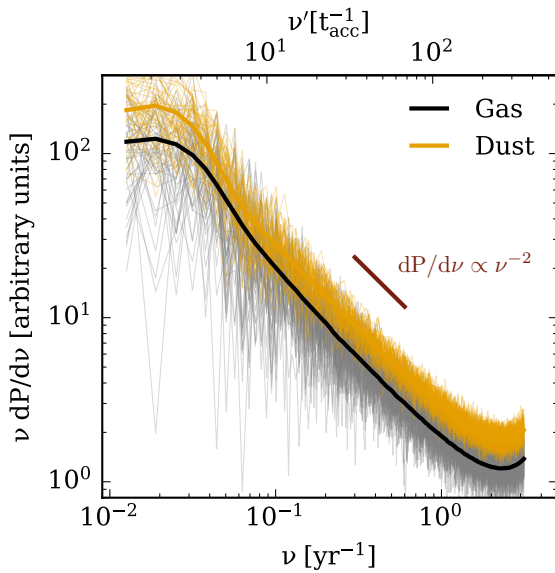


Figure 14. Temporal power spectrum of the gas and dust sightline integrated surface densities along individual sightlines (then lines) as Fig. 11. Thick lines show the average over all sightlines. This is for one RDMHD simulation with initial $N_{\text{H}} \sim 10^{24} \text{ cm}^{-2}$ and $\epsilon_{\text{grain}}^{\text{max}} \sim 0.01 \mu\text{m}$, but others are qualitatively similar. Both the dust and gas show similar profiles, with the dust carrying roughly twice the amount of power as the gas. The spectra show power an approximate red-noise spectrum, $dP/d \ln \nu \propto \nu^{-1}$ over most of the resolvable time range. We expect that the power on long timescales is mostly driven by global processes such as the vertical acceleration of the fluid, and that the power on shorter time-scales is driven by the density fluctuations in the wind.

which power on smaller length-scales would not be resolvable. Thus the power decay on relatively short-length scales should be regarded as a numerical effect, as we expect to continue to rise for smaller length-scales.

3.9.2 Relation to AGN Observations

The RDIs and other instabilities provide a natural explanation for the clumpy nature of the dusty torus, which together with the turbulent dynamics of the fluid, results in variability that is consistent with a large array of AGN observations (Risaliti et al. 2002, 2005; Markowitz et al. 2014; Laha et al. 2020; De Rosa et al. 2007). While the variation we deduce is relatively small, it is non-negligible. We resolve $\sim 10 - 30\%$ variation on scales of few years which would be observable on human timescales. For Compton thick sources, such variability in the gas column would be detectable and significantly change the hardness of the observed X-rays and reduce luminosity by factors of ~ 2 . However, the typical behavior in our simulations would not give rise to variability similar to more extreme changing look AGN which presumably are due to other physics (e.g. accretion disk state changes).

In addition to that, we caution that our findings are sensitive to both the physical size of the line-of-sight/spatial resolution and the temporal resolution of our simulations. When considering observations, the thickness of the line-of-sight is limited by the size of the emitting region, i.e. the angular size of the AGN disk. There-

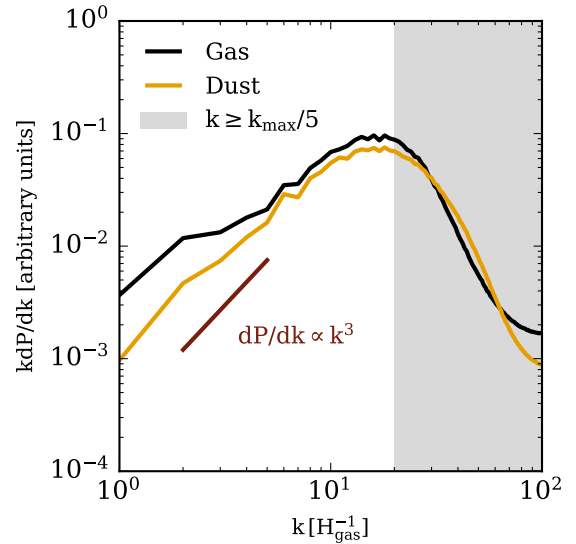


Figure 15. Spatial power spectrum of the three dimensional dust and gas log density fields ($\log(\rho_{\text{gas}} / \langle \rho_{\text{gas}} \rangle)$), ($\log(\rho_{\text{dust}} / \langle \rho_{\text{dust}} \rangle)$). We show this for one simulation with $N_{\text{H}} \sim 10^{24} \text{ cm}^{-2}$ and $\epsilon_{\text{grain}}^{\text{max}} \sim 0.01 \mu\text{m}$ at $t \sim t_{\text{acc}}$, but others are qualitatively similar. The plot shows that similar power for the gas and dust that increases on small scales roughly according to $dP/d \ln k \propto k^2$ until the resolution limit is approached (k_{max} corresponds to the simulation resolution limit), after which due to numerical effects, power on smaller length scales decreases as modes are unresolved.

fore to validate our choice of an infinitesimally narrow line-of-sight for our calculations, we consider the size of the AGN disk relative to the size of the torus. An AGN of luminosity 10^{46} erg/s with a disk emitting black-body radiation peaking in the near-UV regime with effective temperature of $\sim 10^4 \text{ K}$ will have a radius, R_{d} of order $R_{\text{d}} \sim \sqrt{L/4\pi\sigma_{\text{SB}}T^4} \sim 3 \times 10^{-2} \text{ pc}$, where σ_{SB} is the Stefan-Boltzmann constant. Therefore for torus of radius $\sim 1.1 \text{ pc}$, an infinitesimally narrow line-of-sight would be a reasonable approximation to an observationally limited line-of-sight. Regarding the timescales of the variability predicted by our analysis, we note that the shortest timescales we can resolve are limited by the temporal resolution of our output simulation snapshots (\sim years), therefore we are not resolving variability on all human observable timescales, and would expect that there would still be variability due to the RDIs on shorter timescales than those reported in this work. In addition, we note that we expect that the variability that arises due to the RDIs would be much faster than that predicted by an occultation model.

4 CONCLUSIONS

In this work, we present simulations of radiation-dust driven outflows explicitly accounting for dust dynamics and dust-gas radiation-magnetic field-interactions, with initial conditions resembling AGN torii. We model the dust using a realistic grain-size spectrum and grain charge under the influence of a radiation field and accounting for drag and Lorentz forces. The dust interacts with gas through collisional (drag) and electromagnetic (Lorentz, Coulomb) forces, which couple the two fluids, and absorbs radiation which accelerates grains, determining whether they in turn can accelerate gas. While within this environment, the dust and gas are closely coupled in the sense that the “free streaming length” of dust grains is very small, explicit

treatment of dust dynamics reveals that the fluid is unstable on all length-scales to a broad spectrum of fast growing instabilities. We summarize our key findings below.

- (i) **RDI:** The RDIs develop rapidly on scales up to the box size, forming vertical filamentary structures that reach saturation quickly relative to global timescales. We find that the behavior of the RDIs is sensitive to the geometrical optical depth τ_{geo} with environments with higher optical depths resulting in a more tightly coupled dust-gas fluid ($\ell_{\text{stream,dust}}/H_{\text{gas}} \propto \tau_{\text{geo}}^{-1}$), and longer RDI growth times ($t_{\text{grow}}/t_{\text{acc}} \propto \tau_{\text{geo}}^{1/6}$). Other parameters such as AGN luminosity, gravity, grain charging mechanism, and the gaseous equation of state show weaker effects on the dynamics or morphology of the RDIs.
- (ii) **Clustering:** The RDIs drive strong dust-dust and gas-gas clustering of similar magnitude (order of magnitude fluctuations) on small scales for all conditions explored within our parameter set. Thus, the RDIs provide yet another (of many) natural mechanism for explaining the clumpy nature of AGN torii.
- (iii) **Outflows:** Our results show that both the dust and gas are accelerated to highly super-sonic velocities resulting in a wind which can successfully eject 70 – 90% of the gas present. In addition, the RDIs drive super-Alfvénic velocity dispersion of order $\sim 10\%$ of the outflow velocity. Further, while the morphological structure of the RDIs generates low opacity channels through which photons can in principle escape, we find that this “leakage” is modest, usually resulting in less than a factor of ~ 3 loss of photon momentum relative to the ideal case. In every case, the remaining momentum (for quasar-like conditions modeled here) is more than sufficient to drive a wind.
- (iv) **Integrated Surface Density Variation:** The resulting morphology and turbulence gives rise to both short (\leq years) and long timescale (10-100 years) variability in the column density of gas and surface density/opacity of dust integrated along mock observed lines-of-sight to the quasar accretion disk. These fluctuations have RMS amplitude along a given sightline of order $\sim 10 - 20\%$ over year to decade timescales with a red noise power spectrum, consistent with a wide array of AGN observations. We note that both the dust and gas show variability on similar timescales that roughly follow similar trends statistically, but do not match 1-to-1 at any given time — they fluctuate relative to one another, providing a natural explanation for systems where dust extinction is observed to vary in the optical/NIR independent of the gas-dominated x-ray obscuration and vice versa (Risaliti et al. 2002, 2005; Markowitz et al. 2014; Laha et al. 2020; De Rosa et al. 2007; Smith & Vaughan 2007).

ACKNOWLEDGMENTS

Support for for NS and PFH was provided by NSF Research Grants 1911233, 20009234, 2108318, NSF CAREER grant 1455342, NASA grants 80NSSC18K0562, HST-AR-15800. Numerical calculations were run on the Caltech compute cluster “Wheeler,” allocations AST21010 and AST20016 supported by the NSF and TACC, and NASA HEC SMD-16-7592.

DATA AVAILABILITY STATEMENT

The data supporting this article are available on reasonable request to the corresponding author.

REFERENCES

Alonso-Herrero A., et al., 2011, *ApJ*, 736, 82
Antonucci R. R. J., 1982, *Nature*, 299, 605

- Apai D. A., Lauretta D. S., 2010, *Protoplanetary Dust: Astrophysical and Cosmochemical Perspectives*. Cambridge University Press, Cambridge, UK; eds.: D. Apai, D. S. Lauretta
- Assef R., et al., 2018, *The Astrophysical Journal*, 866, 26
- Bai X.-N., Stone J. M., 2010, *ApJ*, 722, L220
- Baloković M., et al., 2018, *ApJ*, 854, 42
- Baskin A., Laor A., 2018, *MNRAS*, 474, 1970
- Bianchi S., Piconcelli E., Chiaberge M., Bailón E. J., Matt G., Fiore F., 2009, *ApJ*, 695, 781
- Caplar N., Lilly S. J., Trakhtenbrot B., 2017, *The Astrophysical Journal*, 834, 111
- Carballido A., Stone J. M., Turner N. J., 2008, *MNRAS*, 386, 145
- Chan C.-H., Krolik J. H., 2016, *ApJ*, 825, 67
- Costa T., Rosdahl J., Sijacki D., Haehnelt M. G., 2018, *MNRAS*, 473, 4197
- De Rosa A., Piro L., Perola G., Capalbi M., Cappi M., Grandi P., Maraschi L., Petrucci P., 2007, *Astronomy & Astrophysics*, 463, 903
- Debuhr J., Quataert E., Ma C., Hopkins P., 2010, *MNRAS*, 406, L55
- Dorschner J., 2003, in Henning T. K., ed., *Lecture Notes in Physics*, Berlin Springer Verlag Vol. 609, *Astromineralogy; University Observatory Schillergässchen 3, D-07745 Jena, Germany*. pp 1–54
- Draine B. T., 2003, *ARA&A*, 41, 241
- Draine B. T., Lee H. M., 1984, *ApJ*, 285, 89
- Draine B. T., Sutin B., 1987, *ApJ*, 320, 803
- Elitzur M., Shlosman I., 2006, *ApJ*, 648, L101
- Elvis M., 2000, *ApJ*, 545, 63
- Elvis M., Marengo M., Karovska M., 2002, *ApJ*, 567, L107
- Gallerani S., et al., 2010, *A&A*, 523, A85
- Grudić M. Y., Guszejnov D., Hopkins P. F., Offner S. S. R., Faucher-Giguère C.-A., 2021, *Monthly Notices of the Royal Astronomical Society*, 506, 2199
- Hatziminaoglou E., Fritz J., Jarrett T., 2009, *MNRAS*, 399, 1206
- Hickox R. C., Alexander D. M., 2018, *ARA&A*, 56, 625
- Höfner S., Olofsson H., 2018, *A&ARv*, 26, 1
- Hon W. J., Webster R., Wolf C., 2020, *Monthly Notices of the Royal Astronomical Society*
- Hönig S. F., 2019, *ApJ*, 884, 171
- Hönig S. F., Kishimoto M., 2010, *A&A*, 523, A27
- Hopkins P. F., 2015, *MNRAS*, 450, 53
- Hopkins P. F., 2016, *MNRAS*, 462, 576
- Hopkins P. F., 2017, *MNRAS*, 466, 3387
- Hopkins P. F., Grudić M. Y., 2019, *MNRAS*, 483, 4187
- Hopkins P. F., Lee H., 2016, *MNRAS*, 456, 4174
- Hopkins P. F., Raives M. J., 2016, *MNRAS*, 455, 51
- Hopkins P. F., Squire J., 2018a, *MNRAS*, 479, 4681
- Hopkins P. F., Squire J., 2018b, *MNRAS*, 480, 2813
- Hopkins P. F., et al., 2004, *AJ*, 128, 1112
- Hopkins P. F., Grudić M. Y., Wetzel A., Kereš D., Faucher-Giguère C.-A., Ma X., Murray N., Butcher N., 2020a, *MNRAS*, 491, 3702
- Hopkins P. F., Squire J., Seligman D., 2020b, *MNRAS*, 496, 2123
- Hopkins P. F., Rosen A. L., Squire J., Panopoulou G. V., Soliman N. H., Seligman D., Steinwandel U. P., 2022, *Monthly Notices of the Royal Astronomical Society*, 517, 1491
- Horst H., Gandhi P., Smette A., Duschl W. J., 2008, *A&A*, 479, 389
- Ishibashi W., Fabian A. C., 2015, *Monthly Notices of the Royal Astronomical Society*, 451, 93
- Ishibashi W., Fabian A. C., Maiolino R., 2018, *MNRAS*, 476, 512
- Ji S., Squire J., Hopkins P. F., 2021, arXiv e-prints, p. arXiv:2112.00752
- Johansen A., Youdin A., Mac Low M.-M., 2009, *ApJ*, 704, L75
- Kawakatu N., Wada K., Ichikawa K., 2020, *ApJ*, 889, 84
- Kishimoto M., Hönig S. F., Antonucci R., Barvainis R., Kotani T., Tristram K. R. W., Weigelt G., Levin K., 2011, *A&A*, 527, A121
- Konigl A., Kartje J. F., 1994, *ApJ*, 434, 446
- Krolik J. H., Begelman M. C., 1988, *The Astrophysical Journal*, 329, 702
- Krumholz M. R., Thompson T. A., 2012, *ApJ*, 760, 155
- Kuiper R., Klahr H., Beuther H., Henning T., 2012, *A&A*, 537, A122
- LaMassa S. M., et al., 2015, *The Astrophysical Journal*, 800, 144
- Laha S., Markowitz A. G., Krumpe M., Nikutta R., Rothschild R., Saha T., 2020, *The Astrophysical Journal*, 897, 66

- Laor A., Draine B. T., 1993, *ApJ*, **402**, 441
- Lawrence A., Elvis M., 1982, *ApJ*, **256**, 410
- Lee H., Hopkins P. F., Squire J., 2017, *MNRAS*, **469**, 3532
- Lupi A., Volonteri M., Silk J., 2017, *MNRAS*, **470**, 1673
- Lupi A., Bovino S., Capelo P. R., Volonteri M., Silk J., 2018, *MNRAS*, **474**, 2884
- MacLeod C. L., et al., 2012, *The Astrophysical Journal*, **753**, 106
- Maiolino R., Schneider R., Oliva E., Bianchi S., Ferrara A., Mannucci F., Pedani M., Roca Sogorb M., 2004, *Nature*, **431**, 533
- Markowitz A., Krumpe M., Nikutta R., 2014, *Monthly Notices of the Royal Astronomical Society*, **439**, 1403
- Mathis J. S., Rumpl W., Nordsieck K. H., 1977, *ApJ*, **217**, 425
- Mathur S. u., et al., 2018, *The Astrophysical Journal*, **866**, 123
- McElroy R., et al., 2016, *Astronomy & Astrophysics*, **593**, L8
- McKinnon R., Vogelsberger M., Torrey P., Marinacci F., Kannan R., 2018, *MNRAS*, **478**, 2851
- Moseley E. R., Squire J., Hopkins P. F., 2019, *MNRAS*, **489**, 325
- Murray N., Quataert E., Thompson T. A., 2005, *ApJ*, **618**, 569
- Nenkova M., Sirocky M. M., Ivezić Ž., Elitzur M., 2008a, *The Astrophysical Journal*, **685**, 147
- Nenkova M., Sirocky M. M., Nikutta R., Ivezić Ž., Elitzur M., 2008b, *The Astrophysical Journal*, **685**, 160
- Netzer H., 2015, *Annual Review of Astronomy and Astrophysics*, **53**, 365
- Norman C., Scoville N., 1988, *ApJ*, **332**, 124
- Padovani P., et al., 2017, *A&ARv*, **25**, 2
- Pan L., Padoan P., Scalo J., Kritsuk A. G., Norman M. L., 2011, *ApJ*, **740**, 6
- Paolillo M., Schreier E., Giacconi R., Koekemoer A., Grogin N., 2004, *The Astrophysical Journal*, **611**, 93
- Paolillo M., et al., 2017, *Monthly Notices of the Royal Astronomical Society*, **471**, 4398
- Pier E. A., Krolak J. H., 1992, *ApJ*, **399**, L23
- Ricci C., et al., 2017, *Nature*, **549**, 488
- Risaliti G., Elvis M., Nicastro F., 2002, *ApJ*, **571**, 234
- Risaliti G., Elvis M., Fabbiano G., Baldi A., Zezas A., 2005, *ApJ*, **623**, L93
- Ross N. P., Graham M. J., Calderone G., Ford K. S., McKernan B., Stern D., 2020, *Monthly Notices of the Royal Astronomical Society*, **498**, 2339
- Roth N., Kasen D., Hopkins P. F., Quataert E., 2012, *ApJ*, **759**, 36
- Ruan J. J., et al., 2016, *The Astrophysical Journal*, **826**, 188
- Runnoe J. C., et al., 2016, *Monthly Notices of the Royal Astronomical Society*, **455**, 1691
- Sanders D. B., Soifer B. T., Elias J. H., Madore B. F., Matthews K., Neugebauer G., Scoville N. Z., 1988, *ApJ*, **325**, 74
- Seligman D., Hopkins P. F., Squire J., 2019a, *MNRAS*, **485**, 3991
- Seligman D., Hopkins P. F., Squire J., 2019b, *MNRAS*, **485**, 3991
- Shen X., Hopkins P. F., Faucher-Giguère C.-A., Alexander D. M., Richards G. T., Ross N. P., Hickox R. C., 2020, *MNRAS*, **495**, 3252
- Smith R., Vaughan S., 2007, *Monthly Notices of the Royal Astronomical Society*, **375**, 1479
- Squire J., Hopkins P. F., 2018a, *MNRAS*, **477**, 5011
- Squire J., Hopkins P. F., 2018b, *ApJ*, **856**, L15
- Squire J., Moroianu S., Hopkins P. F., 2022, *MNRAS*, **510**, 110
- Stalevski M., Fritz J., Baes M., Nakos T., Popović L. Č., 2012, *MNRAS*, **420**, 2756
- Steinwandel U. P., Kaurov A. A., Hopkins P. F., Squire J., 2021, *arXiv e-prints*, p. [arXiv:2111.09335](https://arxiv.org/abs/2111.09335)
- Stern D., et al., 2018, *The Astrophysical Journal*, **864**, 27
- Su K.-Y., Hopkins P. F., Hayward C. C., Faucher-Giguère C.-A., Kereš D., Ma X., Robles V. H., 2017, *MNRAS*, **471**, 144
- Thompson T. A., Quataert E., Murray N., 2005, *ApJ*, **630**, 167
- Thompson T. A., Fabian A. C., Quataert E., Murray N., 2015, *Monthly Notices of the Royal Astronomical Society*, **449**, 147
- Tielens A. G. G. M., 2005, *The Physics and Chemistry of the Interstellar Medium*. Cambridge, UK: Cambridge University Press
- Trakhtenbrot B., et al., 2019, *The Astrophysical Journal*, **883**, 94
- Tristram K., et al., 2007, *Astronomy & Astrophysics*, **474**, 837
- Tristram K. R. W., et al., 2009, *A&A*, **502**, 67
- Tsang B. T.-H., Milosavljević M., 2015, *MNRAS*, **453**, 1108
- Urry C. M., Padovani P., 1995, *Publications of the Astronomical Society of the Pacific*, **107**, 803
- Uttley P., McHardy I. M., 2004, *Progress of Theoretical Physics Supplement*, **155**, 170
- Wada K., 2012, *ApJ*, **758**, 66
- Wada K., Papadopoulos P. P., Spaans M., 2009, *ApJ*, **702**, 63
- Wang J., Xu D., Wei J., 2018, *The Astrophysical Journal*, **858**, 49
- Wise J. H., Abel T., Turk M. J., Norman M. L., Smith B. D., 2012, *MNRAS*, **427**, 311
- Yang Q., et al., 2018, *The Astrophysical Journal*, **862**, 109

APPENDIX A: LIST OF SIMULATIONS

Name	$N_{\text{H}}[\text{cm}^{-2}]$	$\epsilon_{\text{grain}}^{\text{max}}[\mu\text{m}]$	$\tilde{\alpha}_{\text{m}}$	$\tilde{\phi}_{\text{m}}$	$\tilde{g}[10^5]$	$\tilde{a}_{\text{d}}[10^9]$	β^0	Notes
n1e22_eps1	1e+22	1	6.5e-3	27.0	5.7	0.11	0.13	default
n1e22_eps0.1		0.1	6.5e-4	270.0	5.7	1.1	0.13	10x smaller $\epsilon_{\text{grain}}^{\text{max}}$
n1e22_eps0.01		0.01	6.5e-5	2700.0	5.7	11.0	0.13	100x smaller $\epsilon_{\text{grain}}^{\text{max}}$
n1e22_eps1_rhd		1	1e-2	10	1	0.05	1	default RDMHD
n1e22_eps1_rhd_c		1	1e-2	10	1	0.05	1	RDMHD - no RSOL ($\tilde{c} = c$)
n1e22_eps1_rhd_hr		1	1e-2	10	1	0.05	1	RDMHD - higher spatial resolution
n1e22_eps1_rhd_modB		1	6.5e-3	27.0	5.7	0.11	0.13	RDMHD - weaker \mathbf{B}^0
n1e22_eps1_rhd_modB_lr		1	6.5e-3	27.0	5.7	0.11	0.13	RDMHD - weaker \mathbf{B}^0 & lower spatial resolution
n1e24_eps1	1e+24	1	6.5e-5	2.7	5.7	0.11	0.13	default
n1e24_eps0.1		0.1	6.5e-6	27.0	5.7	1.1	0.13	10x smaller $\epsilon_{\text{grain}}^{\text{max}}$
n1e24_eps0.01		0.01	6.5e-7	270.0	5.7	11.0	0.13	100x smaller $\epsilon_{\text{grain}}^{\text{max}}$
n1e24_eps0.01_hr_t		0.01	6.5e-7	270.0	5.7	11.0	0.13	higher temporal resolution
n1e24_eps0.01_lr		0.01	6.5e-7	270.0	5.7	11.0	0.13	lower spatial resolution
n1e24_eps0.01_xlr		0.01	6.5e-7	270.0	5.7	11.0	0.13	much lower spatial resolution
n1e24_eps1_rhd		1	1e-4	1	1	0.05	1	default RDMHD
n1e24_eps1_rhd_c		1	1e-4	1	1	0.05	1	No RSOL ($\tilde{c} = c$)
n1e24_eps1_rhd_fw		1	6.5e-4	2.7	5.7	0.02	1	lower F_{rad} & stronger \mathbf{g}
n1e25_eps1	1e+25	1	6.5e-6	0.85	5.7	0.11	0.13	default
n1e25_eps0.1		0.1	6.5e-7	8.5	5.7	1.1	0.13	10x smaller $\epsilon_{\text{grain}}^{\text{max}}$
n1e25_eps0.01		0.01	6.5e-8	85.0	5.7	11.0	0.13	100x smaller $\epsilon_{\text{grain}}^{\text{max}}$
n1e25_eps1_rhd		1	1e-5	0.32	1	0.05	1	default RDMHD
n1e25_eps1_rhd_fw		1	6.5e-6	0.85	5.7	0.02	0.13	lower F_{rad} & stronger \mathbf{g}
n1e26_eps1	1e+26	1	6.5e-7	0.27	5.7	0.11	0.13	default
n1e26_eps0.1		0.1	6.5e-8	2.7	5.7	1.1	0.13	10x smaller $\epsilon_{\text{grain}}^{\text{max}}$
n1e26_eps0.01		0.01	6.5e-9	27.0	5.7	11.0	0.13	100x smaller $\epsilon_{\text{grain}}^{\text{max}}$
n1e26_eps1_rhd_c		1	1e-6	0.1	1	0.05	1	default RDMHD
n1e26_eps1_rhd_hr		1	1e-6	0.1	1	0.05	1	RDMHD - higher spatial resolution
n1e26_eps1_rhd		1	1e-6	0.1	1	0.05	1	RDMHD - higher spatial resolution & RSOL
n1e26_eps1_rhd_modB		1	6.5e-7	0.27	5.7	0.11	0.13	weaker \mathbf{B}^0

Table A1. Initial conditions for all simulations. The simulations organized by the gas column density, and dashed lines separate simulations using the uniform flux approximation from the RDMHD runs. Columns show: (1) Simulation name. (2) Physical column density of the gas: N_{gas} . (3) Physical size of the largest grains: ϵ_{grain} . (4) Grain charge parameter $\tilde{\phi}_{\text{m}} \equiv 3 Z_{\text{grain}}^0 [\epsilon_{\text{grain}}^{\text{max}}] e / (4 \pi c (\epsilon_{\text{grain}}^{\text{max}})^2 \rho_{\text{base}}^{1/2})$ of the largest grains. (5) Grain-size parameter $\tilde{\alpha}_{\text{m}} \equiv (\tilde{\rho}_{\text{grain}}^i \epsilon_{\text{grain}}^{\text{max}}) / (\rho_{\text{base}} H_{\text{gas}})$ of the largest grains. (6) Gravity parameter $\tilde{g} \equiv |\mathbf{g}| H_{\text{gas}} / c_s^2$. (7) Dust acceleration parameter: $\tilde{a}_{\text{d}} \equiv (3/4) (F_0 \langle Q \rangle_{\text{ext}} / c) / (\rho_{\text{base}} c_s^2)$. (8) Initial plasma $\beta_0 \equiv (c_s / v_A^0)^2$. (9) Notes for each run and key differences relative to its corresponding default run.